

# Insight Into Supersonic Combustion Using High-order Simulations

**Ioannis Kokkinakis**

University of Nicosia

**Dimitris Drikakis** (✉ [drikakis.d@unic.ac.cy](mailto:drikakis.d@unic.ac.cy))

University of Nicosia

**Yun-qin He**

Beihang University

**Guo-zhu Liang**

Beihang University

---

## Research Article

**Keywords:** supersonic combustion, high-order simulations, Propulsion, scramjet technologies

**Posted Date:** January 7th, 2022

**DOI:** <https://doi.org/10.21203/rs.3.rs-1214905/v1>

**License:** © ⓘ This work is licensed under a Creative Commons Attribution 4.0 International License.

[Read Full License](#)

---

# Insight into supersonic combustion using high-order simulations

Ioannis W. Kokkinakis<sup>1</sup>, Dimitris Drikakis<sup>1,\*</sup>, Yun-qin He<sup>2</sup>, and Guo-zhu Liang<sup>2</sup>

<sup>1</sup>University of Nicosia, Nicosia CY-2417, Cyprus

<sup>2</sup>Beihang University, Beijing 100191, China

\*drikakis.d@unic.ac.cy

## ABSTRACT

High-order simulations of supersonic combustion are presented to advance understanding of the complex chemically-reacting flow processes and identify unknown mechanisms of the high-speed combustion process. We have employed 11th-order accurate implicit large-eddy simulations in conjunction with thermochemistry models comprising 20 chemical reactions. We compare the computations with available experiments and discuss the accuracy and uncertainties in both. Jets emanating from above and below the hydrogen plumes influence the combustion process and accuracy of the predictions. The simulations reveal that high temperatures are sustained for a long-distance downstream of the combustion onset. A barycentric map for the Reynolds stresses is employed to analyse the turbulent anisotropy. We correlate the axisymmetric contraction and expansion of turbulence with the interaction of reflected-shock waves with the supersonic combustion hydroxyl production regions. The physics insights presented in this study could potentially lead to more efficient supersonic combustion and scramjet technologies.

## Introduction

Propulsion is one of the critical components for achieving sustainable future hypersonic flights. Turbojets have been successfully used in aircraft flying in the transonic and supersonic region up to Mach 3. However, conventional aero-propulsion engines (e.g., turbofan & turbojet) cannot withstand temperatures occurring at higher speeds. Alternatively, ramjets can be used for Mach numbers in the range of 3 to 5. Although the vehicle's speed is supersonic, the engine design forces the flow to become subsonic through a series of shockwaves and compression waves. This results in high pressures and temperatures, thus eliminating the need for a compressor altogether prior to the combustion of the fuel. When increasing the flight speed yet further, eventually the ramjet too becomes inefficient because the losses in the engine dramatically increase – the inlet temperature gets closer to the exhaust temperature so less energy can be extracted in the form of thrust. The simplest alternative, therefore, is for the incoming air to not be compressed (and hence heated) as much. Consequently, however, the air flowing through the combustion chamber will still be travelling very fast relative to the engine. In fact, the flow in the combustion chamber will be supersonic –hence the name supersonic-combustion ramjet, or scramjet–, resulting in a low temperature air that rapidly mixes with the fuel. The whole reaction process is completed inside the engine, e.g., Fig 1. As per above, scramjet engines typically allow for Mach speeds in the range of 6 to 15. Both ramjet and scramjet engines have no moving parts, making them attractive for supersonic and hypersonic flight.

Scramjet engines encompass many complexities associated with high thermal and structural loads, short fuel residence times, and high viscous drag<sup>1,2</sup>. However, their development relies mainly on ground test facilities, which cannot replicate the actual operational flight conditions. Furthermore, the cost for facilities that can replicate total pressure and enthalpies for scramjet flight altitudes and speeds is exceptionally high, thus the limited number of such facilities worldwide. Various methodologies have been proposed to reduce the requirements, e.g., direct connect testing, where the facility reproduces the equivalent conditions at the combustor entrance; and semi-free jet testing, where the facility produces the flow behind the forebody shock<sup>3</sup>. However, the above approaches cannot account for phenomena occurring upstream of the combustion, such as the ingestion of hypersonic boundary layers, transition to turbulence, forebody shock, and flow spillage.

To achieve sustainable, commercial hypersonic flights would require advancing our understanding of the scramjet combustion processes. The above would require a synergetic approach between experimental testing and computational fluid dynamics (CFD), aero propulsion simulations. Researchers have looked into various aspects of scramjet combustion phenomena. These include the mechanism of detonation propagation; shock impingement at the inlet; flame acceleration and deflagration to detonation transition; solid-fueled scramjets; supersonic hydrogen jet in a crossflow configuration; computational analysis of high-speed combustors, such as HyShot II and the DLR experimental rig, and staggered ramp and strut injector configurations<sup>4-11</sup>.

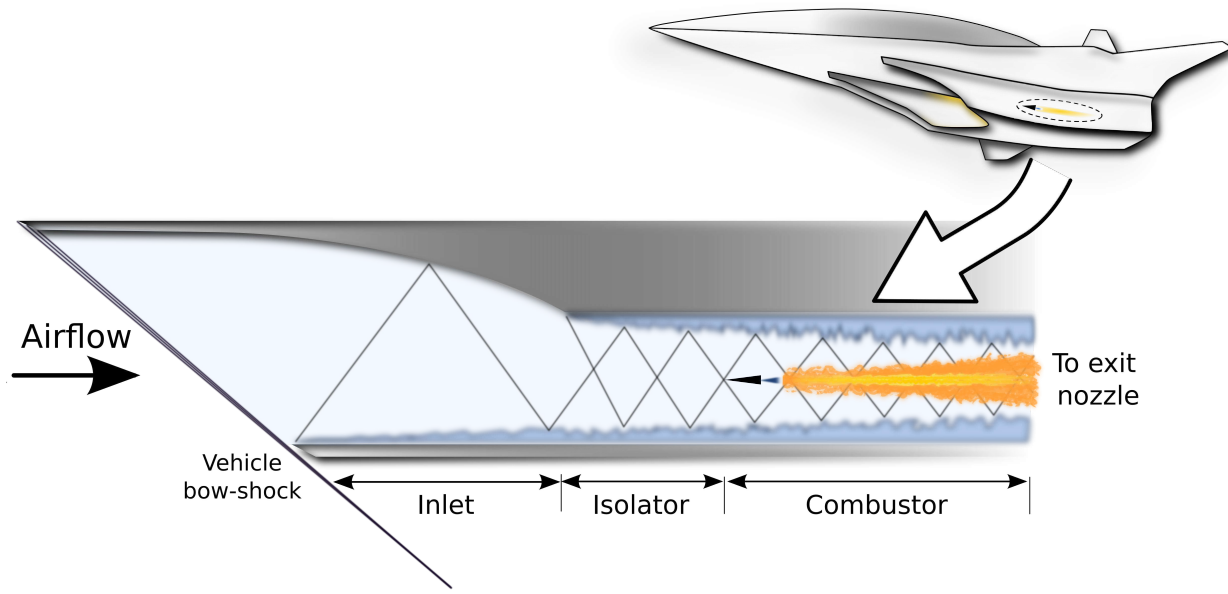


**Figure 1.** Schematic of the scramjet engine of a fictional hypersonic vehicle illustrating the combustor region considered in this study.

Due to the extreme flow environment, experimental measurements are difficult to be obtained and encompass many uncertainties. Computational Aerospace Propulsion (CAP) provides a powerful framework for advancing the design and development of scramjet engines. CAP can give insight into the details of the flow and chemistry in different parts of the domain, can provide data for quantities that are limited by instrumentation, and can help repeat computations at a reduced cost compared to ground test facilities. However, it also encompasses numerical and physics modelling challenges for supersonic combustion. Ideally, one wants to reduce uncertainty by making simulations and experiments to converge to the same, or very similar, answer.

The recent development of very high-order methods for implicit large-eddy simulations (ILES) of supersonic and hypersonic flows showed promising results<sup>12-14</sup>. Therefore, in this study we employ high-order ILES, 11th-order accurate, to model and simulate the scramjet supersonic combustion process. We aim at shedding light in the flow physics, e.g., by analysing the Reynolds stress anisotropy to identify mechanisms influencing the combustion process and correlate the turbulent anisotropy with the combustion chamber's turbulent contraction and expansion, as well as hydroxyl (OH) production. We believe that these processes could potentially be controlled to help make supersonic combustion more efficient.

### 3D Scramjet combustion

The flow configuration follows the experimental setup at DLR<sup>10</sup> using a typical strut-based injection system in a supersonic combustion ramjet. The side-view schematic of the scramjet combustion chamber is shown in Fig. 2. The preheated vitiated air inlet of this combustor has a height of 50 mm and a width of 40 mm. The upper wall of the combustor has a divergence angle of 3° to compensate for the boundary-layer growth. The wedge is 32 mm long, and its half-angle is 6°. At the centre of the base of the wedge, hydrogen at sonic condition (Mach 1) is injected into a Mach 2 supersonic preheated airflow through 15 holes of diameter 1 mm and 2.4 mm apart. For the simulation presented here, three of the holes were simulated. The total length and width of the computational zone are 340 mm and 7.2 mm, respectively. The flow conditions of the incoming vitiated air stream and the hydrogen jet are given in Table 1. Note that the time-step size for the simulation was of the order of  $\mathcal{O}(10^{-8})$  sec, despite not resolving the viscous no-slip surfaces.

Previous computational and experimental comparisons for the DLR supersonic combustion experiment show that the experimental root mean square for the velocity is out of the free stream velocity range in some positions. In contrast, computations<sup>4</sup> are closer to the correct speed (about one dimensionless). This is evidence of the challenge of measuring in such extreme flow conditions.

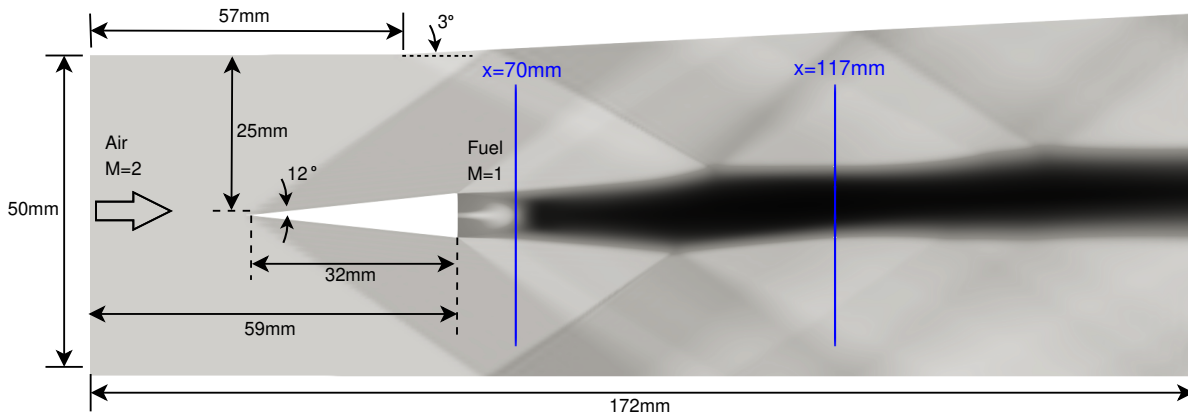


**Figure 2.** Schematic of scramjet domain simulated overlaid with an illustration of the profiles location used in the comparison; background plot of the mean temperature field given for illustration purposes.

Condition	$Ma$	$p$ (bar)	$T$ (K)	$Y_{O_2}$	$Y_{N_2}$	$Y_{H_2O}$	$Y_{H_2}$
Air	2	1	340	0.232	0.736	0.032	0
Fuel ( $H_2$ )	1	1	250	0	0	0	1

**Table 1.** Inflow conditions of hydrogen fuel and atmospheric air for the DLR<sup>10</sup> scramjet case configuration.

### Computational methods accuracy

According to Fig. 3, the distance from the  $H_2$  jet exit outlet at which combustion is sustained is considerably further downstream for both the 2<sup>nd</sup>- (M2LM) and 5<sup>th</sup>-order (M5LM) MUSCL limiters. Moreover, it was observed that without augmenting the 2<sup>nd</sup>-order MUSCL limiter with the low-Mach number correction (as per §), the flame would not be sustained and would eventually extinguish. Although the flow is predominantly supersonic in the streamwise direction, applying the low-Mach number correction reduces the numerical dissipation of the fluxes along the vertical path and the subsonic region behind the wedge. The resulting enhanced turbulence that is resolved is more effective in mixing the air with the hydrogen fuel and reducing the mean streamwise velocity.

Arguably, the downstream position at which the flame initiates and is sustained is one of the most challenging and critical flow properties necessary to be accurately captured. The experiment indicates –according to the temperature profiles in Figure 4 – that combustion initiates around  $x \leq 70$  mm. Since the 11<sup>th</sup>-order WENO scheme provided the most accurate result, as evident in Fig. 3, all other schemes have been omitted in the subsequent analysis.

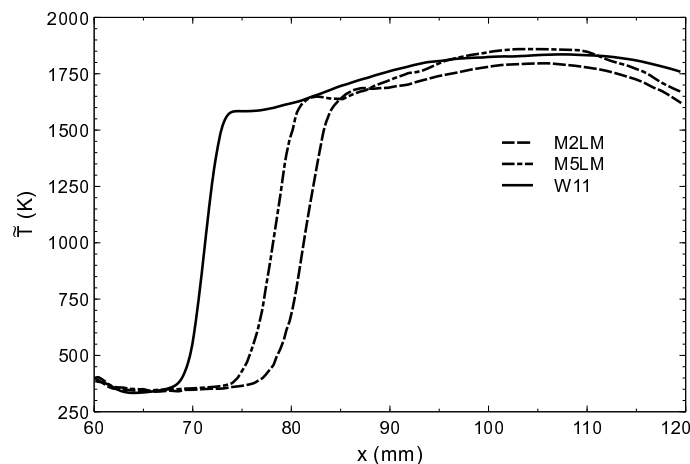


**Figure 3.** Comparison of mean temperature,  $\bar{T}$ , profiles along  $y = 0$ mm, starting from the centre of the  $H_2$  inlet jet at  $x = 59$ mm and up to  $x = 117$ mm.

## Computation vs experiment

We have first performed comparisons against the experimental results bearing in mind the uncertainties about experimental measurements and matching the exact initial conditions between experiments and simulations.

The mean axial velocity,  $\langle \tilde{u}_x \rangle$ , obtained using the high-order ILES, compares overall favourably to the experiment DLR<sup>10</sup> at two different locations,  $x = 70\text{mm}$  (upper graph) and  $x = 117\text{mm}$  (lower graph) (first column in Fig. 4). The experiment shows a higher mean axial velocity in the vicinity of the hydrogen jet plume  $y/L = 0$  for  $x = 70\text{ mm}$ , and slower at  $x = 117\text{mm}$ .

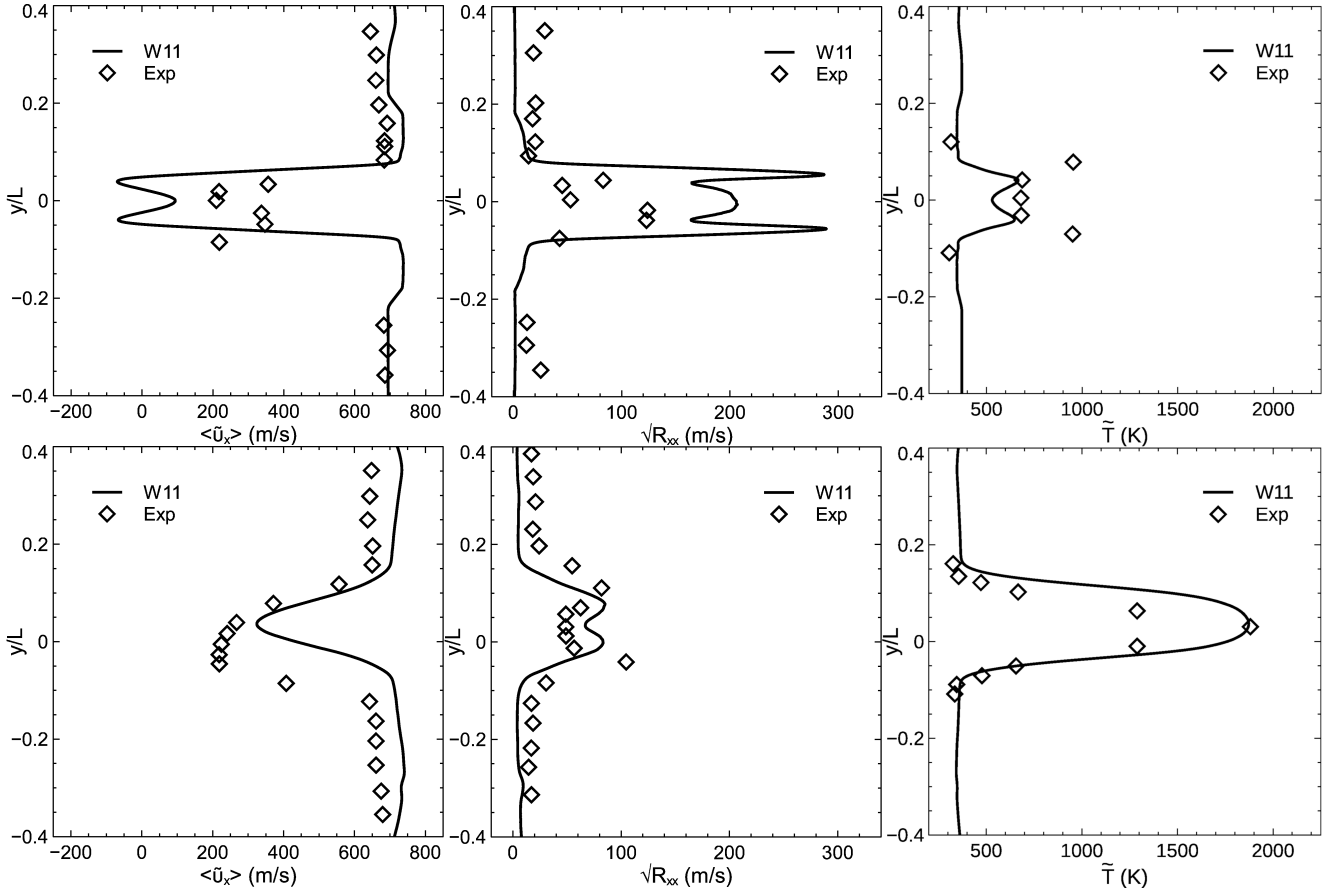


**Figure 4.** Comparison of the mean axial velocity ( $\langle \tilde{u} \rangle$  column 1), mean RMS axial velocity ( $\langle \widetilde{u''u''} \rangle^{1/2}$  column 2), mean temperature ( $\langle \tilde{T} \rangle$  column 3), profiles at different streamwise locations; upper row  $x = 70\text{mm}$ , and lower row  $x = 117\text{mm}$ .

The root-mean-square (RMS) profiles of the streamwise velocity fluctuations are shown in the second column of Fig. 4. Above and below the mixing and combustion region,  $|y/L| > 0.1$ , the streamwise velocity RMS is smaller in the simulations at both locations ( $x = 70\text{mm}$  &  $x = 117\text{mm}$ ), suggesting either an issue with the calibration of the experimental measuring devices or, more likely, the presence of significant velocity fluctuations in the incoming flow of the experiment. This result suggests that either the inflow fluctuations upstream of the wedge or (and) the boundary layer characteristics in the inclined surfaces of the strut/wedge and combustor walls are not accurately represented in the simulation as they were in the actual experiment. The above is part of the uncertainty of validating such flows. Unless the experiment could measure and provide such information, a mismatch in the comparisons should be expected. At  $x = 160\text{mm}$ , the predicted RMS agrees much better with the experiment, particularly at the strut's wake.

The mean temperature,  $\langle \tilde{T} \rangle$ , is underpredicted in the simulation at  $x = 70\text{mm}$ , however, this is commonplace among computational studies<sup>15–19</sup> of the particular experiment<sup>10</sup>. On the other hand, at  $x = 117\text{mm}$ , the mean temperature profile compares favourably with that of the experiment. The agreement of the peak value, in particular, indicates that the thermochemistry numerical solver can accurately model the heat released from the combustion of the injected hydrogen fuel with the Oxygen in the free-stream air.

The main conclusions from the mean flow comparisons between simulations and experiments are:

1. There is overall a good agreement between simulation and experiment.
2. The mean temperature profile at  $x = 117\text{mm}$  appears to diffuse more in the simulations than the experiment, i.e., in terms of its shape (or distribution). However, the opposite is the case for the mean axial velocity and RMS.
3. At  $x = 70\text{mm}$ , the temperature in the strut's wake is under-predicted while the mean axial velocity and RMS are over-predicted.

The shape and dynamics of the recirculation bubbles that form in the strut's wake may improve if the turbulent boundary layer over the upper and lower inclined strut/wedge surfaces and the upper and lower shear layers formed just after the strut corner edges are resolved. Therefore, an even better agreement between the experimental and numerical results may be plausible. However, this would be at the expense of enormous computational cost due to the increase in the number of points required to conduct wall-resolved simulations.

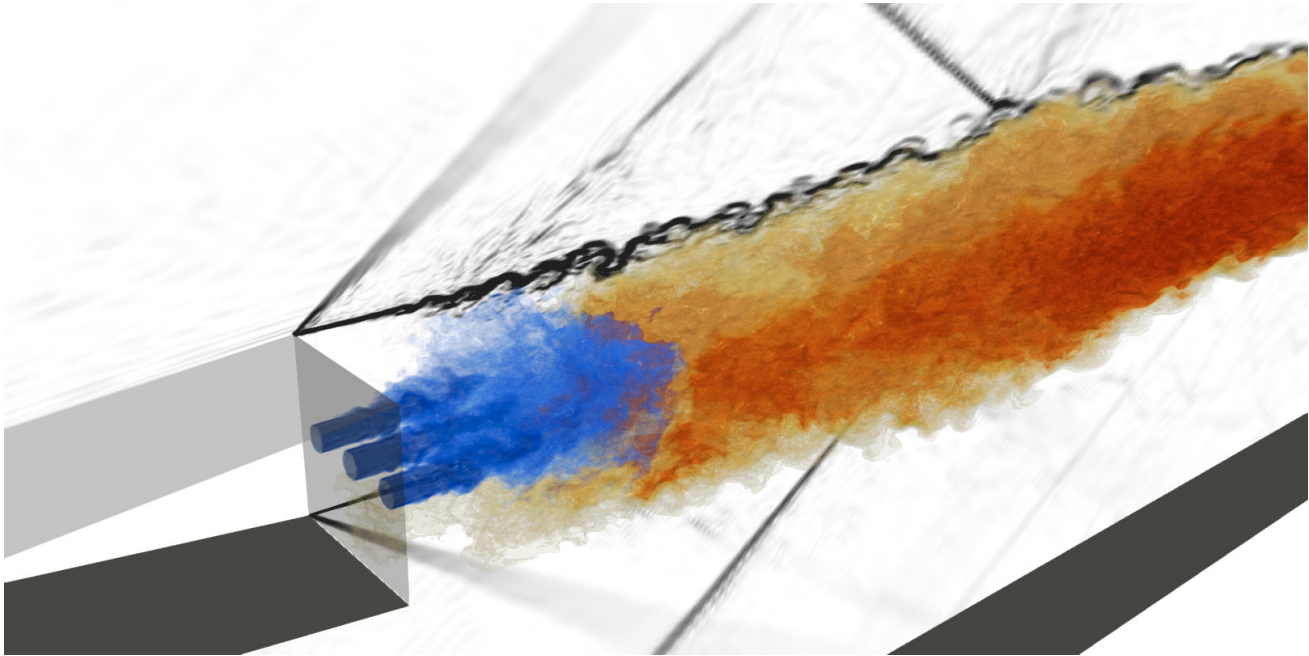


**Figure 5.** Illustration of an instantaneous snapshot of the three-dimensional flow; Blue:  $\text{H}_2$  fuel mass fraction ( $Y_{\text{H}_2} = 0.4 - 1.0$ ); Yellow-Orange: Temperature ( $T = 500 - 2000\text{K}$ ); background contour plane of the density gradient magnitude  $|\nabla\rho|$ .

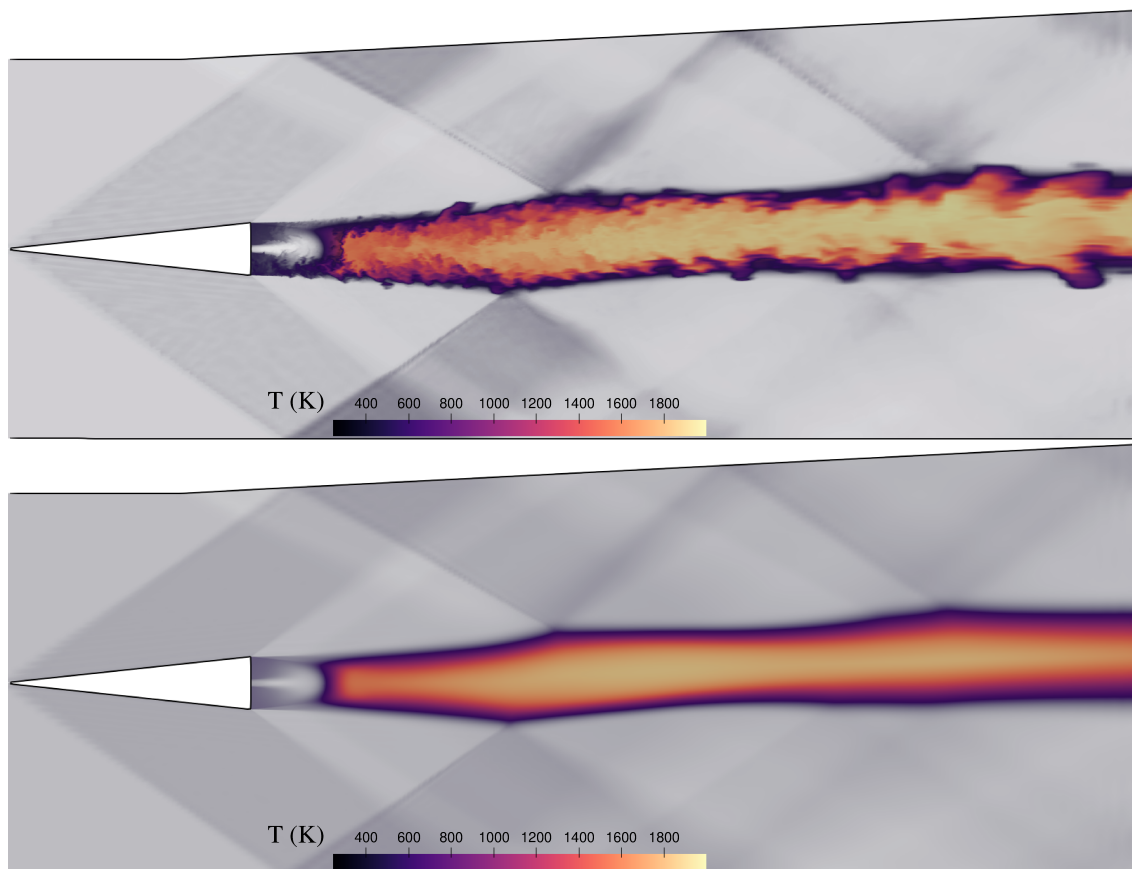
## Flow field structure

We present the 3D flow (Figure 5) using renderings of the instantaneous temperature,  $T$ , and hydrogen fuel mass-fraction,  $Y_{\text{H}_2}$ , iso-surfaces, providing a qualitative understanding of the flow. The blue mist-like iso-surfaces signify a mass-fraction of  $Y_{\text{H}_2} \geq 0.5$ , while the solid iso-surface (mostly visible at the hydrogen fuel inlets) indicates a mass-fraction of  $Y_{\text{H}_2} = 1$ . Regarding the flame, the yellow iso-surface indicates a temperature of  $500\text{K}$ , while the darker orange has a temperature of  $2,000\text{K}$ . The high temperature is influenced by the two merging shockwaves at that location, as Fig. 2 suggests. The 3D iso-surface image and the 2D contour plots show the short time and distance over which the ignition takes place, causing the temperature to increase rapidly thereafter (Fig. 6). Temperatures as high as  $2000$  Kelvin are maintained for a long distance downstream of the combustion onset (Fig. 6).

The simulation shows that the flame can propagate upstream towards the wedge, either from below or above the hydrogen plume; the former being the case for the time instance depicted. This phenomenon is responsible for the prominent temperature peaks at the edges of the strut's wake observed in Fig. 4 for  $x = 70\text{mm}$ . Precisely, the entrainment of hydrogen fuel occurs along the upper portion of the plume towards the strut due to a recirculation bubble in the strut's wake (Fig. 5). The hydrogen becomes trapped behind the strut until a sufficient amount of it is accumulated and eventually ignites with the aid of the downstream flame.

A closer inspection of the results reveals the flame moves upstream from above or below the hydrogen plume in an alternating sequence. The enhanced mixing observed above and below the injected hydrogen plume causes the flame propagating upstream and igniting the accumulated hydrogen once it has been sufficiently mixed – via turbulence transport – with Oxygen from the freestream (atmospheric) air. Figure 5 clearly demonstrates the importance of the free shear layer in the mixing rate. The mismatch of computations and experiments at the free shear layer (Fig. 4) could be due to the different resolved frequency or duration of the alternating ignition sequence between the upper and lower free shear layers between experiments and computations.

Neglecting the viscous terms in such simulations subject to high accuracy in the advective terms with the optimal subgrid dissipation for large-eddy simulations does not affect the mixing process between the hydrogen fuel and the atmospheric air in the strut's wake. Notably, the high-order WENO scheme maintained the flame at the correct distance from the strut/wedge as indicated by the experiment, mainly thanks to its superior turbulence resolution. The above further supports that the advective mixing due to the turbulence is dominant over molecular diffusion. Reducing the mismatch of the inflow conditions (velocity perturbations) between experiments and simulations for the bulk flow turbulence intensity will undoubtedly help reduce the prediction uncertainty. Furthermore, resolving the turbulent boundary layer over the strut's surfaces at a more refined (grid-wise) level could further increase the simulation accuracy in the vicinity of the free shear layer. However, this would severely increase the computational cost.



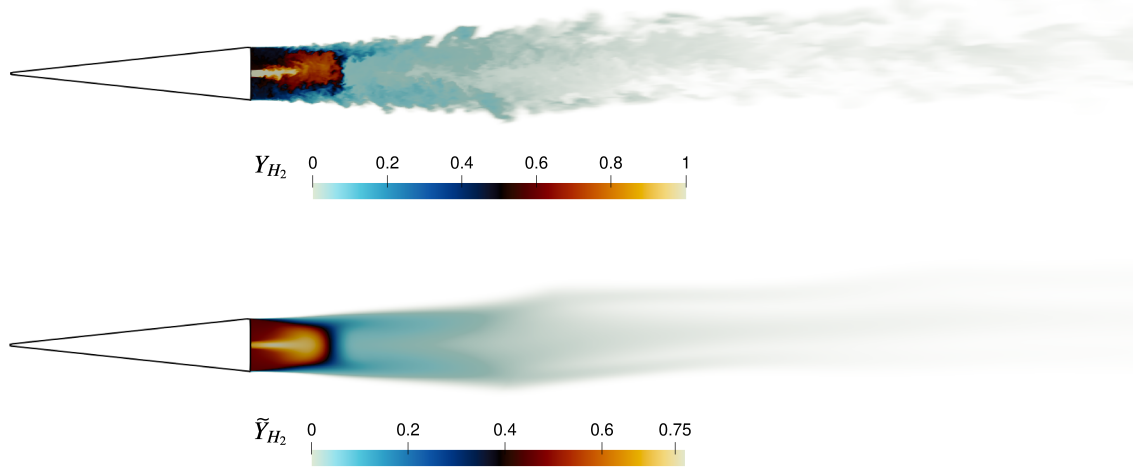
**Figure 6.** Contour plot of an instantaneous 2D snapshot (upper) and the mean (lower) Temperature field in degrees Kelvin.

Figure 6 shows the instantaneous (upper) and mean (lower) temperature fields. The instantaneous contour plot corresponds to the spanwise mid-plane, right through the centre of the second  $H_2$  jet plume visible in Fig. 5.

The combustion takes place just downstream of the  $H_2$  fuel plume breakdown. The upstream propagation of the flame along the lower free shear layer observed in the instantaneous contour plot at a slightly lower temperature relative to the central flame core, approximately 600 – 1500K, depending on the location and the stage of the “burst”. The mean Oxygen-to-Hydrogen mass-fraction ratio in the wake of the strut is generally low, from below 1:10 in the mixing (or free shear) layer to nearly zero in the mid-stream of the plume. Therefore,  $O_2$  alone cannot account for the consumption of the  $H_2$  fuel observed.

For further clarity, we also provide the contour plot of the instantaneous and mean mass-fraction of the  $H_2$  fuel (Fig. 7) as well as hydroxyl (Fig. 8). Particularly the latter component, OH, is an important transient species in Hydrogen-Oxygen

combustion. It contributes significantly to the rate of oxidation and heat release in low-temperature plasma thanks to the relatively fast rate, at low temperature, of exothermic H abstraction by OH, such as the process  $\text{OH} + \text{H}_2 \leftrightarrow \text{H} + \text{H}_2\text{O}$ . It also has a significant presence in the chain-branching reactions for a high-temperature combustion system.



**Figure 7.** Contour plot of the instantaneous (upper) and the mean (lower)  $\text{H}_2$  fuel mass-fraction.

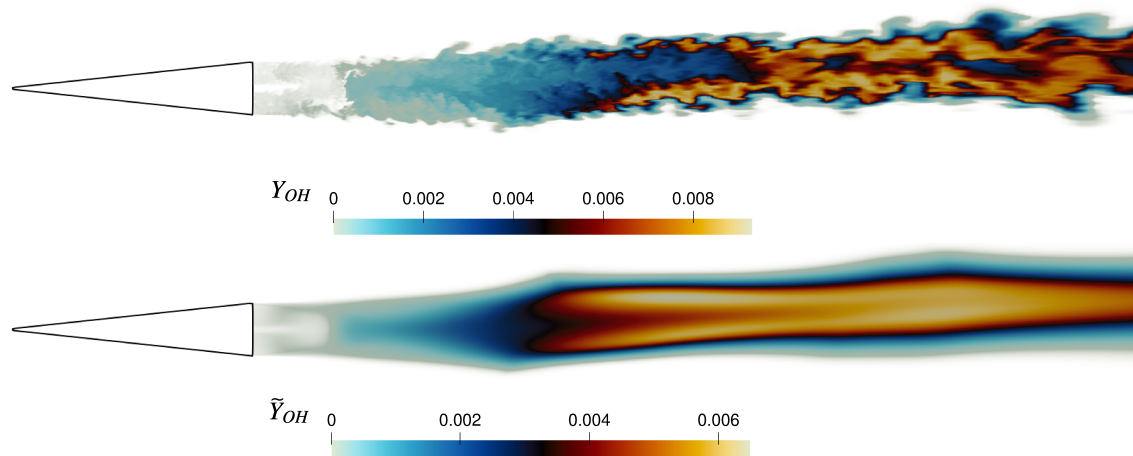


**Figure 8.** Contour plot of the instantaneous (upper) and the mean (lower) OH fuel mass-fraction.

Regarding the  $\text{H}_2$  fuel-injected, its rapid consumption at a short distance from the strut is evident. However, not all of the  $\text{H}_2$  is consumed immediately, with a trace amount burnt gradually downstream of the flame front region. A gradual increase in OH observed along the mixing layer downstream of the flame front appears to correlate well with the consumption of  $\text{H}_2$ , effectively splitting the latter into three streams of trace amounts. Importantly, this occurs at the region where the reflected shocks –emanating from the strut’s leading-edge – converge into the flame’s outer area.

At first glance, it appears as though the  $\text{H}_2$  fuel burns faster at the centre of the main flame front, rather than the outer regions that are richer in  $\text{O}_2$ . However, this is caused by the recirculation bubbles in the strut’s wake and the gradual accumulation of  $\text{H}_2$ . Specifically, the instantaneous plot of the  $\text{H}_2$  mass-fraction clearly shows a small amount released from behind the strut’s upper wake region, along with its corresponding free shear layer. However, in the lower free shear layer, the  $\text{H}_2$  is consumed by the flame propagating upstream towards the strut.

The mean temperature and mass-fraction results in the vicinity of the strut’s wake and the flame front manifest the alternating sequence of the upstream flame bursts between the lower and upper free shear layers.

The temperature increases downstream – particularly along the flame’s inner core region – reaching a peak value of 2,000K despite the trace amounts of  $\text{H}_2$ . The culprit is predominantly the formation and consumption of OH, which is most abundant at the same high-temperature regions. The gradual consumption of OH post both shock–flame interactions (that occur within the computational domain extent employed) is evident and correlates well to the high-temperature regions. Note that the reflected

shock waves will also contribute directly to the temperature rise observed in the shock-flame interaction regions, but to a lesser extent.

The results demonstrate that there are two distinct central flame regions at the vicinity of the ignition front. First, the “inner” region occurs where the main flame ignites as a result of the mixing between the  $H_2$  fuel plume and the atmospheric air transported via the turbulent free shear layer. Second, the “outer” region occurs along (and just below) the upper and lower turbulent free shear (or mixing) layers that form in the strut’s wake, where the concentration of  $O_2$  is the highest. However, the two regions are not entirely distinct, and their dynamical behaviours are intertwined. When the flame propagates upstream and the upper or lower mixing layers, the  $H_2$  jet plume is directed towards the other. As a result, a rich in  $H_2$  flow momentarily forms at the inner flame’s front, causing it to move downstream. However, the  $H_2$  rich flow rapidly mixes with the turbulent free shear layer, predominantly comprised of atmospheric air, and eventually forms a more favourable fuel-to-air ratio causing the inner flame front to move back upstream again. The latter occurs while the flame initially propagates upstream, and the other mixing layer begins to extinguish as the fuel-atmospheric air mix is consumed. Thus, the burnt fuel-air transports downstream before the fuel-to-air ratio improves again and the process is repeated *ad infinitum*.

### Turbulent free shear layer

Figures 9 and 10 depict 3D renderings of the instantaneous temperature,  $T$ , and hydrogen fuel mass-fraction,  $Y_{H_2}$ , iso-surfaces at two different time instances, providing a qualitative understanding of the flow. More specifically, the blue iso-surface signifies  $Y_{H_2} = 0.6$ , while the white iso-surface (mostly visible at the hydrogen fuel inlets) indicates  $Y_{H_2} = 1$ . Regarding the flame, the yellow iso-surface indicates a temperature of 500K, while the dark-red has a temperature of 1,900K. The latter is partly attributed to the two merging shockwaves at that location, as Fig. 2 suggests. The 3D iso-surface images help illustrate how short of a time and distance combustion takes place, causing the temperature to increase rapidly.

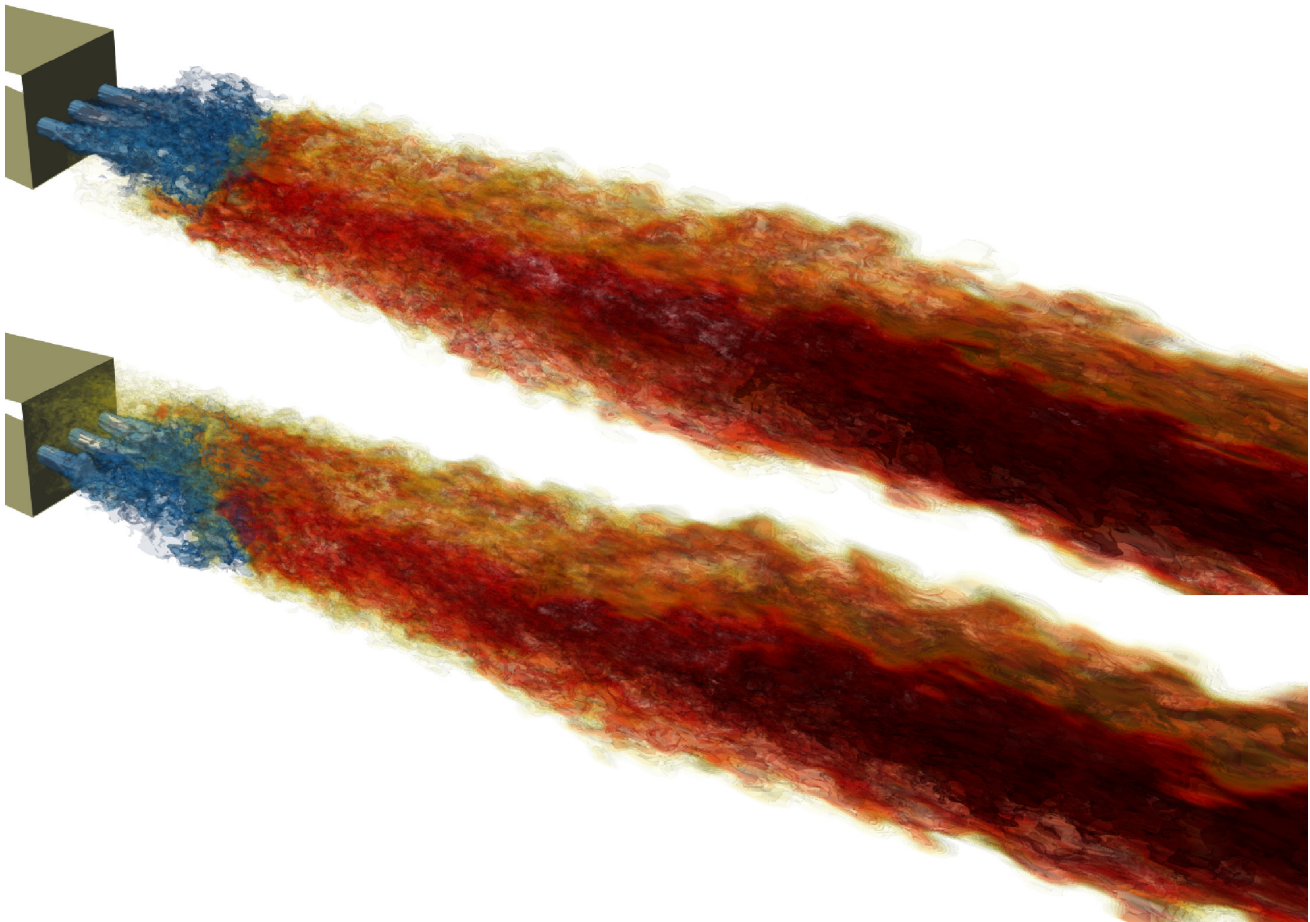


**Figure 9.** Iso-surfaces of  $H_2$  fuel (white-blue), and temperature (yellow-red-black) at two different time instances; isometric view.

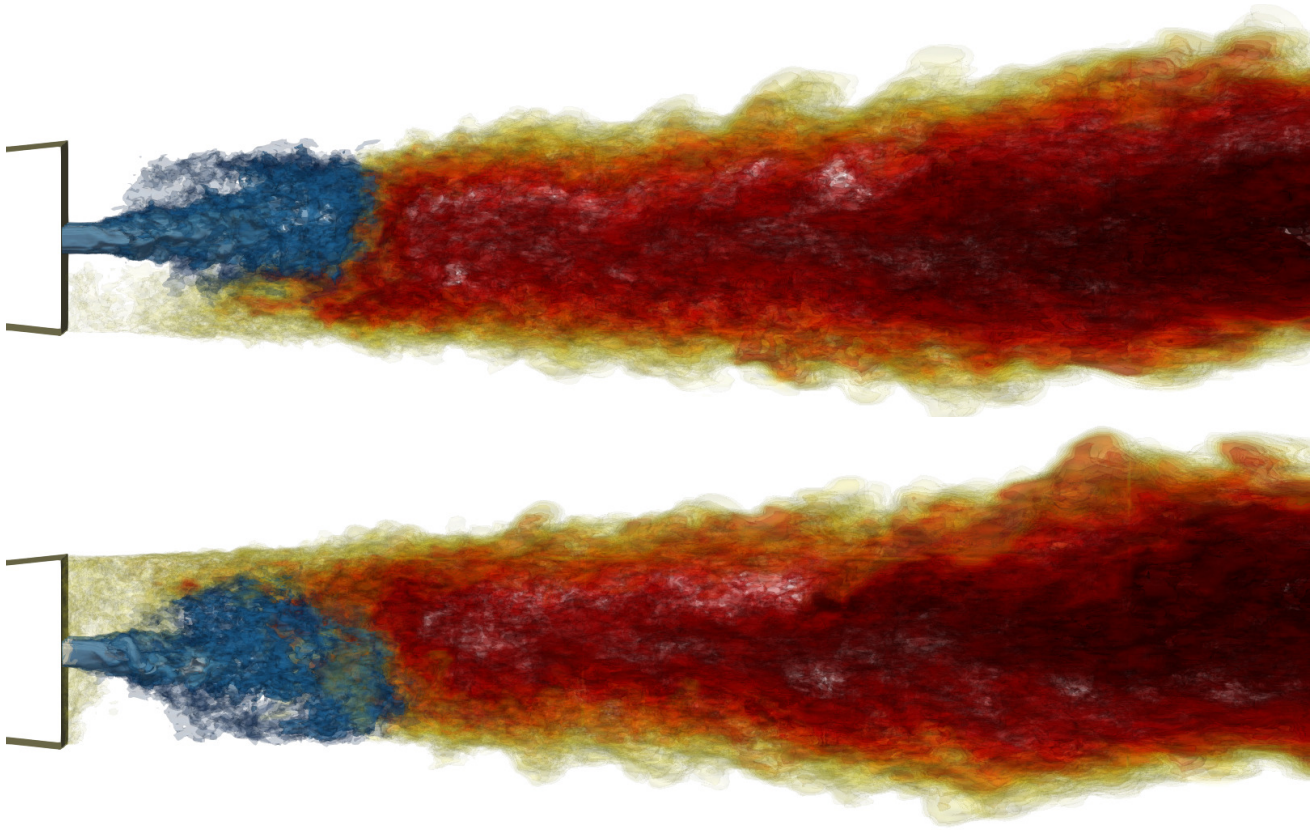


**Figure 10.** Iso-surfaces of  $H_2$  fuel mass-fraction (white-blue), and temperature (yellow-red-black) at two different time instances;  $xy$  orthographic view.

Moreover, the 3D visualizations clearly show that the flame can propagate upstream towards the wedge below or above the hydrogen plume. This phenomenon is responsible for the prominent temperature peaks at the edges of the strut's wake that can be seen in Fig. 4. More specifically, in Fig. 10, entrainment of hydrogen fuel can be seen moving along the upper portion of the plume towards the strut due to a recirculation bubble in the strut's wake. The hydrogen becomes trapped behind the strut until a sufficient amount of it is accumulated that ignites the downstream flame.

A closer inspection of the computational data reveals that the flame moves upstream from above and below the hydrogen plume in an alternating sequence. A possible explanation for the under-prediction of the temperature at the shear layer, as indicated in Fig. 4, could be that the resolved frequency of the alternating sequence is lower than the experimental. Again, the lack of resolving the turbulent boundary layer along the wedge and the subsequent shear layer is an attributing cause. Furthermore, we should consider that the experiment also encompasses several uncertainties that deserve further investigation. Figure 10 in particular, helps illustrate the importance that the under-resolved shear layer has on the flow evolution and behaviour at this crucial region.

The temperature variation over time is extracted at two points, either one positioned between one of two free-shear layers and the hydrogen plume, i.e., at  $(x, y) = (64, \pm 3)$  mm on the mid-plane ( $z = 3.6$  mm). The signals' power spectrum density (PSD) is calculated and shown in Fig. 11. A peak at  $\simeq 7,990$  Hz is apparent, corresponding to the frequency at which the free-shear layers periodically ignite, while the layers ignition is out of phase by  $180^\circ$ .

In conclusion, due to the very high Reynolds number of the case, neglecting the viscous terms did not adversely affect the mixing processes between the hydrogen fuel and the atmospheric air in the strut's wake. Notably, the high-order WENO scheme maintained the flame at the correct distance from the strut/wedge as indicated by the experiment, mainly thanks to its superior turbulence resolution. The above further supports that the advective mixing due to the turbulence is dominant over that using molecular diffusion. Though considering the bulk flow turbulence and turbulent boundary layer could further increase the simulation accuracy in the vicinity of the shear layer, this will be at the cost of severely increased computational demand.

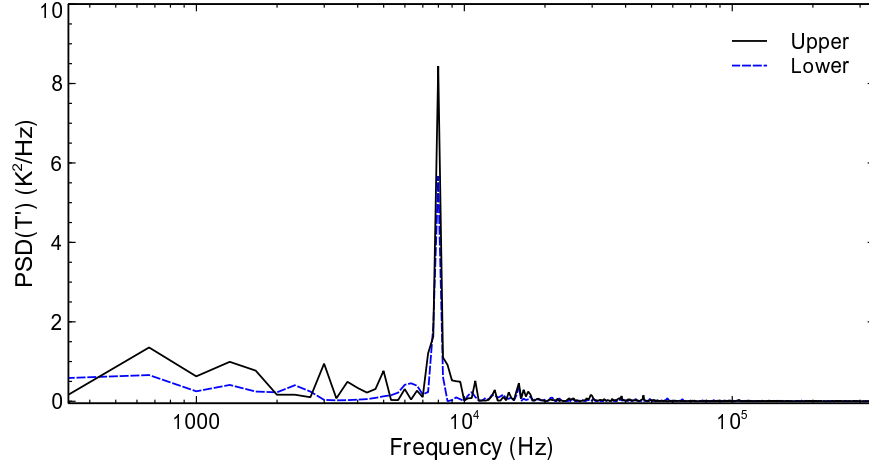


**Figure 11.** Power spectrum density of temperature at just below the upper and lower turbulent free-shear layers; points positioned on the mid-plane,  $z = 3.6$  mm, at  $(x, y) = (64, \pm 3)$  mm.

## Reynolds stress anisotropy

This study also sheds light on another aspect of flow physics. We have investigated the turbulence anisotropy using the barycentric map method<sup>20</sup>. We have implemented a modified map form to clarify the different turbulence anisotropy states<sup>21</sup>. A description of the procedure follows.

The Reynolds stress,  $R_{ij}$ , and the Reynolds stress anisotropy tensor,  $a_{ij}$ , are calculated according to:

$$R_{ij} = \overline{u_i' u_j'} = \overline{\rho u_i' u_j'} / \bar{\rho} \quad (1)$$

and

$$a_{ij} = \frac{R_{ij}}{2k} - \frac{\delta_{ij}}{3}, \quad \text{where } k = \frac{R_{kk}}{2}$$

The three eigenvalues of the  $a_{ij}$  (diagonal) tensor are obtained such that  $\lambda_1 \geq \lambda_2 \geq \lambda_3$ .

The eigenvalues are used to position the turbulence field on the barycentric anisotropy invariant map. The eigenvalues lie in the interval  $-1/3 \leq \lambda_i \leq 2/3$ , and the number of non-zero eigenvalues and equalities between them identify the limiting states of anisotropy. Based on their visual description, the limiting states are spherical, pancake-like and rod or cigar-like turbulence.

The first state corresponds to a three-component state, which is the isotropic turbulence, i.e.,  $X_{3c}$  ( $\lambda_1 = \lambda_2 = \lambda_3 = 0$ ). The fluctuations are of equal magnitude and occur in all directions. Another state is the isotropic two-component turbulence  $X_{2c}$  ( $\lambda_1 = \lambda_2 = 1/6, \lambda_3 = -1/3$ ). In this case, fluctuations of equal magnitude occur in two directions. The last limiting state is one-component turbulence  $X_{1c}$  ( $\lambda_1 = 2/3, \lambda_2 = \lambda_3 = -1/3$ ), which describes a flow where turbulent fluctuations only exists along one direction.

A convex combination of the above limiting states can describe any turbulence state. An equilateral triangle is constructed to visualise the barycentric map. The peaks of the graph represent the limiting states (Fig. 12). Thus, we can identify both the intensity and the type of turbulence anisotropy. A modified weights estimate is used to distinguish further the different transition regions between the three limiting states of anisotropy:

$$X_{ic} = (C_{ic} + C_{off})^{C_{exp}} \quad (2)$$

where

$$C_{1c} = \lambda_1 - \lambda_2, \quad C_{2c} = 2(\lambda_2 - \lambda_3), \quad C_{3c} = 3\lambda_3 + 1$$

and  $C_{off} = 0.65$  and  $C_{exp} = 5$ .

The sides of the triangle (map boundaries) define the transition regions. The right side of the triangle, coloured magenta in Fig. 12, corresponds to axisymmetric expansion in which one diagonal component of the Reynolds stress tensor is larger than the other two, equal components. Thus, turbulence has a prolate spheroid shape. In the scramjet, the axisymmetric expansion is the predominant turbulence anisotropy state in the strut's wake and the flame region. It also occurs in the regions where (i)

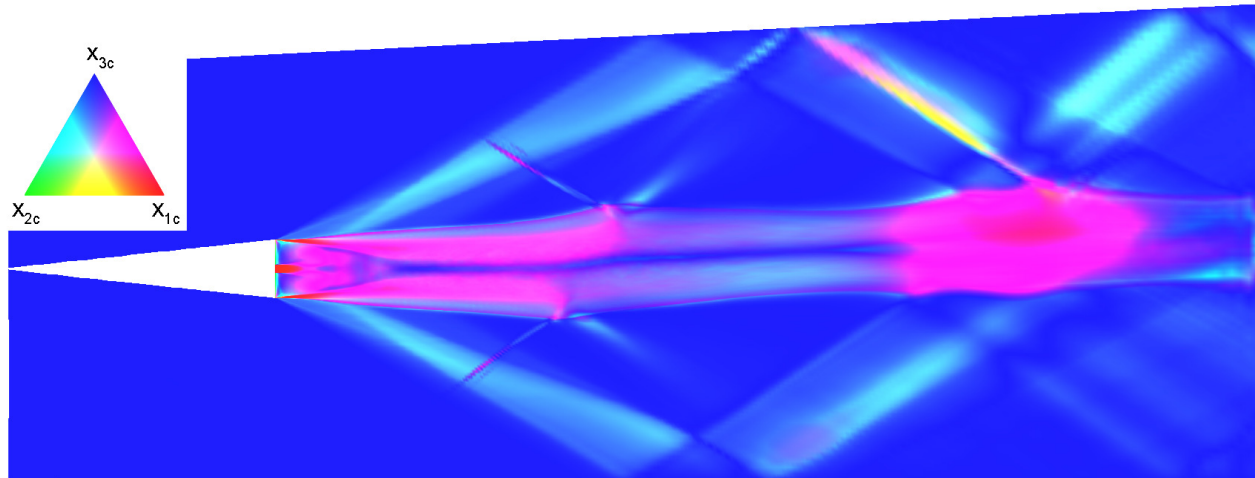


**Figure 12.** Contour plot of the Reynolds stress anisotropy componentality using Eq. (2) with  $C_{\text{off}} = 0.65$  and  $C_{\text{exp}} = 5$ .

the strut's leading-edge reflected shock waves from the walls interact with the flame; (ii) the  $\text{H}_2$  jet plume breaks down into turbulence and undergoes mixing, and (iii) the turbulent free shear layers emanate from the corner edges of the wedge-shaped strut.

In all of the above cases, the predominant Reynolds stress component of the axisymmetric expansion is the normal streamwise component,  $R_{11}$ . Overall, the shock interactions and turbulent free shear layers make the turbulence state more anisotropic. Note that the turbulence anisotropy state development of the turbulent free shear layers closely matches that observed in non-reacting compressible but subsonic, free shear layers for a sudden-expansion geometry<sup>22</sup>. However, the axisymmetric turbulence state at the hydrogen's plume mixing region transforms to an isotropic turbulence state at the flame's front. The sudden volumetric expansion that occurs as a result of the combustion initiation and rapid heating leads to a decrease of the predominant incoming normal streamwise Reynolds stress component,  $R_{11}$ . The reduction is so pronounced that a steep drop in the turbulence kinetic energy also occurs.

The left side of the triangle, coloured cyan, represents an axisymmetric contraction in which one component is smaller than the other two parts, which are equal. The shape of turbulence is an oblate spheroid. The axisymmetric contraction of turbulence is correlated mainly with the location of the expansion waves. Note that because no turbulence intensity was considered in the upstream air in this study, turbulence fluctuations remained relatively weak upstream of the strut. Consequently, no upstream nonlinear waves are visible in Fig. 12—they are extremely steady. However, the two free shear layers that form at the strut's wake are both turbulent and the mixing that ensues downstream of the  $\text{H}_2$  injector outlets. The subsequent interaction of the nonlinear waves with the strut's turbulent wake induces to the former an unsteady motion, causing their appearance on the anisotropy componentality map. Moreover, axisymmetric contraction can be observed along the region of hydroxyl (OH) production Fig. 8, indicating that the chemical reactions processes here are likely different and, importantly, affect the turbulence differently.

Another important observation is the “reaction” of turbulent flow to the second shock-flame interaction (Fig. 12). The turbulence state in the entire surrounding region is transformed towards an axisymmetric expansion due to an increase in the  $R_{11}$  component. Closer inspection shows that the increase occurs due to the turbulence flame interacting with the reflected expansion waves rather than the reflected shock waves. The latter causes a decrease in  $R_{11}$ , such that a near isotropic turbulence state occurs in the immediate vicinity downstream.

The two-component turbulence is shown at the bottom side of the triangle (in yellow). It can be visualised as an ellipse and is typically present near the walls where the wall-normal component of the fluctuations vanishes much faster than the other parts. The two-component turbulence also appears in the region of the reflected shock waves on the upper side of the domain. It is caused by interacting with the reflected expansion waves.

## Conclusions

The key findings from the present study are summarised below:

1. High-order simulations of supersonic combustion processes can shed light on the physics of the flow and combustion that the experiment may not visualise and measure due to the extreme environment inside the scramjet. Specifically, the

simulations show the fluid jets emanating from around the hydrogen plumes influencing the combustion process and the high temperatures. Furthermore, the simulations provide information about turbulent anisotropy.

2. The shear layers above and below the fuel region are associated with strong turbulence anisotropy (axisymmetric expansion).
3. The shock waves, reflecting from the wall and interacting with the flame, further result in a region of strong anisotropy.
4. The above event is also associated with hydroxyl production.
5. The highest mean temperature,  $\bar{T}$ , occurs shortly after the first shock-flame interaction, where an oval shaped region between 1,840–1,880 K forms starting at  $(x, y) \simeq (98.5, 0.9)$  mm, ending at  $(x, y) \simeq (125, 2.1)$  mm, and of a maximum thickness of  $\approx 2.36$  mm.
6. Small “pockets” of instantaneous temperature,  $T \simeq 1,900$  K occur within the region of the highest *mean* temperature,  $\bar{T}$ . However, the highest *instantaneous* temperature range of 1,950–2000 K is found to be at the second shock-flame interaction, i.e.,  $(x, y) \simeq (134, 3.1)$ – $(162, 4.8)$  mm, and of a maximum thickness of  $\approx 7$  mm.
7. The predictions show that the H<sub>2</sub> fuel is consumed within a short distance from its injector outlets, approximately 13 mm.
8. The flame propagates upstream along with both turbulent free-shear layers at a frequency of  $\simeq 7,990$  Hz, while the two are out of phase by 180°.
9. The computational and experimental results are within the same range and overall in good agreement. However, one should consider that uncertainties arise from the mismatch of initial and boundary conditions between experiments and simulations, e.g., the spanwise periodicity (3 holes vs 15), inlet condition (turbulence intensity), etc.
10. Resolving finer details of the corners around the scramjet edge and wall boundary layer would enable further physics details. However, this would be at the expense of significantly higher computational costs. Furthermore, it remains to be seen that such a demanding simulation would alter the above findings regarding the supersonic combustion processes.

We suggest that it is worth investigating the shear layers above and below the fuel plume and the shock/flame interaction, particularly in the light of the turbulence anisotropy finding in these regions revealed in the present study.

## Methods

### Governing equations

Modelling detonation problems requires the use of the compressible Navier–Stokes equations in conjunction with complex chemistry:

$$\frac{\partial \rho}{\partial t} = -\nabla \cdot (\rho \mathbf{u}) \quad (3)$$

$$\frac{\partial \rho \mathbf{u}}{\partial t} = -\nabla \cdot (\rho \mathbf{u} \otimes \mathbf{u}) - \nabla p + \nabla \cdot \boldsymbol{\tau} + \rho \mathbf{b} \quad (4)$$

$$\frac{\partial \rho e_t}{\partial t} = -\nabla \cdot (\rho \mathbf{u} h_t) + \nabla \cdot (\mathbf{u} \cdot \boldsymbol{\tau}) + \rho \mathbf{u} \cdot \mathbf{b} + \nabla \cdot (k \nabla T) + \nabla \cdot \left[ \sum_{j=1}^{N_{sp}} (h_j \rho D_j \nabla Y_j) \right] - \sum_{j=1}^{N_{sp}} (\rho h_j \dot{\omega}_j) \quad (5)$$

$$\frac{\partial \rho Y_j}{\partial t} = -\nabla \cdot (\rho Y_j \mathbf{u}) + \nabla \cdot (\rho D_j \nabla Y_j) + \rho \dot{\omega}_j, \quad (6)$$

where  $h_t = e_t + p/\rho$  is the total specific enthalpy,  $k = c_p \mu / Pr$  is the thermal conductivity,  $D_j = \mu_j / (\rho Sc_j)$  is the  $j^{\text{th}}$  species mass diffusivity,  $\boldsymbol{\tau} = \mu \left[ \nabla \otimes \mathbf{u} + (\nabla \otimes \mathbf{u})^T - (2/3) (\nabla \cdot \mathbf{u}) \mathbf{I} \right]$  is the viscous stress tensor,  $\mu$  is the dynamic viscosity,  $Pr$  and  $Sc$  are the Prandtl and Schmidt numbers, respectively. No body forces have been considered in this study, i.e.,  $\mathbf{b} = 0$ . The energy equation includes the inter-diffusional enthalpy flux arising from the species mixing<sup>23</sup>. The species equations includes the rates that account for the complex chemistry (combustion).

## Chemical reaction kinetics

### Rates-of-change

Due to the chemical reaction(s), the individual species mass, as well as the mixture energy, will change. The chemical reactions are summarised in Table 2. The following ODE describe the rates at which these take place:

$$(\dot{Y}_j) \sim \frac{dY_j}{dt} = \dot{\omega}_j \quad (7)$$

$$\rho(\dot{h}) \sim \rho c_p \frac{dT}{dt} = - \sum_j \left( \frac{\rho}{\mathcal{M}_j} \dot{\omega}_j H_{m,j} \right), \quad (8)$$

where  $H_{m,j} = h_j/n_j$  is the *molar enthalpy* of the  $j^{\text{th}}$  species, while the *specific enthalpy* (per unit mass) is:

$$h_j = \frac{H_j}{m_j} = \frac{H_j}{n_j \mathcal{M}_j} = \frac{H_{m,j}}{\mathcal{M}_j}$$

where  $n_j = \chi_j n$ , and  $\chi_j$  is the molar-fraction of the  $j^{\text{th}}$  species. The specific enthalpy is defined as  $h = e_i + p/\rho = \gamma e_i$ , where  $e_i = c_v T = p/[\rho(\gamma - 1)]$  is the specific internal energy; hence also  $h = c_p T = \gamma c_v T \equiv \gamma e_i$ . The molar mass of substance  $j$  is defined as  $\mathcal{M}_j = m_j/n_j$ , therefore Eq. (8) can be written as:

$$\rho c_p \frac{dT}{dt} = - \sum_j^{N_{sp}} (\rho \dot{\omega}_j h_j)$$

Note that the mass-fraction,  $Y_j$ , and temperature,  $T$ , ODE required to be solved for complex chemistry are:

$$\frac{dY_j}{dt} = \dot{\omega}_j \quad (9)$$

$$c_p \frac{dT}{dt} = - \sum_j^{N_{sp}} (\dot{\omega}_j h_j), \quad (10)$$

where  $c_p$  is the *specific heat capacity* at constant pressure of the mixture.

### Progress rates

The mass reaction-rate of species  $j$  is the sum of all contributions from the elementary reactions:

$$\dot{\omega}_j = \frac{\mathcal{M}_j}{\rho} \sum_{i=1}^{N_{re}} (v'_{ij} - v''_{ij}) r_i \quad (11)$$

The progress rate  $r_i$  of the  $i^{\text{th}}$  reaction is defined as

$$r_i = k_{f,i} \prod_{j=1}^{N_{sp}} c_j^{n'_{ij}} - k_{r,i} \prod_{j=1}^{N_{sp}} c_j^{n''_{ij}}, \quad (12)$$

where  $c_j$  denotes the molar concentration of the species  $j$ ,  $k_{f,i}$  and  $k_{r,i}$  the forward and reverse constants of the  $i^{\text{th}}$  reaction, and exponents  $n'_{ij}$  and  $n''_{ij}$  are equal to coefficients  $v'_{ij}$  and  $v''_{ij}$ , respectively, if the  $i^{\text{th}}$  reaction describes a true molecular process. Note that  $v'_{ij}$  and  $v''_{ij}$  are the stoichiometric coefficients of species  $j$  appearing as a reactant and as a product, respectively, in reaction  $i$ .

Usually, the forward constants  $k_{f,i}$  are functions of temperature  $T$  and species concentrations  $c_j$ . The particular expressions for forward constant  $k_{f,i}$  are different for different chemical models. However, chemical models mostly used in combustion share the same description of elementary chemical reactions, based on the modified Arrhenius law, leading to a rate coefficient expressed as:

$$k_{f,i} = A_i T^{\beta_i} \exp\left(-\frac{E_i}{R_u T}\right) \quad (13)$$

, with  $A_i$  the pre-exponential factor,  $\beta_i$  the temperature exponent and  $E_i$  the activation energy of the  $i^{\text{th}}$  reaction. The forward and reverse constants of the reaction are linked by the equilibrium constant  $K_{e,i}$ :

$$K_{e,i} = \frac{k_{f,i}}{k_{r,i}} \quad (14)$$

that is expressed by:

$$K_{e,i} = \left( \frac{P_{\text{atm}}}{R_u T} \right)^{\sum_{j=1}^{N_{sp}} (v'_{ij} - v''_{ij})} \exp \left( \frac{\Delta S_{m,i}}{R_u} - \frac{\Delta H_{m,i}}{R_u T} \right) \quad (15)$$

The parameters  $\Delta S_{m,i}$  and  $\Delta H_{m,i}$  correspond to the ideal gas molar entropy and enthalpy change, respectively, during the transition from reactants to products for the  $i^{\text{th}}$  reaction. These quantities are obtained from tabulations based on experimental measurements and/or theory.

For numerical simulations of reacting flows, a chemical scheme is required. Therefore, we must determine the knowledge of all species and reactions before the computation can be carried out.

### Thermodynamics

The non-dimensional heat capacities (determined experimentally or theoretically) are approximated with the temperature polynomials given by

$$\frac{C_{pm,j}}{R_u} = \sum_{n=1}^N a_{nj} T^{(n-1)}, \quad (16)$$

where  $C_{pm,j}$  is the molar heat capacity at constant pressure of the  $j^{\text{th}}$  species. The approximation  $C_{pm,j}(T)$  is considered for two temperature ranges and seven coefficients  $a_j$  are needed for each of these ranges. According to Eq. (16), these polynomial approximations take the following form:

$$\frac{C_{pm,j}}{R_u} = a_{1j} + a_{2j}T + a_{3j}T^2 + a_{4j}T^3 + a_{5j}T^4, \quad (17)$$

where the (absolute) temperature is in units of Kelvin.

Other ideal gas thermodynamic properties are given in terms of integrals of the  $C_{pm,j}$ -function. First, the molar enthalpy is defined by

$$H_{m,j} = H_{m,j}^{\circ}(298\text{K}) + \int_{298\text{K}}^T C_{pm,j} dT, \quad (18)$$

so that

$$\frac{H_{m,j}}{R_u T} = \sum_{n=1}^N \frac{a_{nj} T^{(n-1)}}{n} + \frac{a_{N+1,j}}{T}, \quad (19)$$

where the parameter  $a_{N+1,j}$ , represents the standard heat of formation at 298 K; the superscript ( $^{\circ}$ ) indicates conditions at a Standard State, e.g., 1 atm, 298 K, pH 7.

The molar entropy is given by

$$S_{m,j} = S_{m,j}^{\circ}(298\text{K}) + \int_{298\text{K}}^T \frac{C_{pm,j}}{T} dT, \quad (20)$$

so that

$$\frac{S_{m,j}}{R_u} = a_{1j} \ln T + \sum_{n=2}^N \frac{a_{nj} T^{(n-1)}}{(n-1)} + a_{N+2,j}, \quad (21)$$

where the parameter  $a_{N+2,j}$ , represents the standard entropy of formation at 298 K.

### Hydrogen-Oxygen combustion

A total of 9 species ( $\text{H}_2$ ,  $\text{O}_2$ ,  $\text{H}_2\text{O}$ ,  $\text{O}$ ,  $\text{H}$ ,  $\text{OH}$ ,  $\text{HO}_2$ ,  $\text{H}_2\text{O}_2$ ,  $\text{N}_2$ ) and 20 chemical reactions are considered to model the combustion process between the hydrogen fuel and atmospheric air (Table 1). The reduced model reaction set is given in Table 2 for completeness.

The chemical reaction mechanism for hydrogen-oxygen shown in Table 2 is derived by reduction of a more extensive mechanism<sup>24</sup>. It has been validated using software tools for solving complex chemical kinetics problems, e.g. ChemKin, including the burning temperature, ignition delay time, and species molar fractions.

	Reaction	A	B	E
(1)	H+O <sub>2</sub> +M ⇌ HO <sub>2</sub> +M H <sub>2</sub> O / 18.6 / H <sub>2</sub> / 2.86 /	3.61E+17	-0.72	0.0
(2)	2H+M ⇌ H <sub>2</sub> +M	1.0E+18	-1.0	0.0
(3)	2H+H <sub>2</sub> ⇌ 2H <sub>2</sub>	9.2E+16	-0.6	0.0
(4)	2H+H <sub>2</sub> O ⇌ H <sub>2</sub> +H <sub>2</sub> O	6.0E+19	-1.25	0.0
(5)	H+OH+M ⇌ H <sub>2</sub> O+M H <sub>2</sub> O / 5.0 /	1.6E+22	-2.0	0.0
(6)	H+O+M ⇌ OH+M H <sub>2</sub> O / 5.0 /	6.2E+16	-0.6	0.0
(7)	2O+M ⇌ O <sub>2</sub> +M	1.89E+13	0.0	-1788.0
(8)	H <sub>2</sub> O <sub>2</sub> +M ⇌ 2OH+M	1.3E+17	0.0	45500.0
(9)	H <sub>2</sub> + O <sub>2</sub> ⇌ 2OH	1.7E+13	0.0	47780.0
(10)	OH+H <sub>2</sub> ⇌ H <sub>2</sub> O+H	1.17E+9	1.3	3626.0
(11)	O+OH ⇌ O <sub>2</sub> + H	3.61E+14	-0.5	0.0
(12)	O+H <sub>2</sub> ⇌ OH+H	5.06E+4	2.67	6290.0
(13)	OH+HO <sub>2</sub> ⇌ H <sub>2</sub> O+O <sub>2</sub>	7.5E+12	0.0	0.0
(14)	H+HO <sub>2</sub> ⇌ 2OH	1.4E+14	0.0	1073.0
(15)	O+HO <sub>2</sub> ⇌ O <sub>2</sub> +OH	1.4E+13	0.0	1073.0
(16)	2OH ⇌ O+H <sub>2</sub> O	6.0E+8	1.3	0.0
(17)	H+HO <sub>2</sub> ⇌ H <sub>2</sub> + O <sub>2</sub>	1.25E+13	0.0	0.0
(18)	2HO <sub>2</sub> ⇌ H <sub>2</sub> O <sub>2</sub> +O <sub>2</sub>	2.0E+12	0.0	0.0
(19)	H <sub>2</sub> O <sub>2</sub> +H ⇌ HO <sub>2</sub> +H <sub>2</sub>	1.6E+12	0.0	3800.0
(20)	H <sub>2</sub> O <sub>2</sub> +OH ⇌ H <sub>2</sub> O+HO <sub>2</sub>	1.0E+13	0.0	1800.0

**Table 2.** Reduced chemical reaction mechanism (9 species and 20 reactions) used to model air-H<sub>2</sub> combustion. The pre-exponential factor (or frequency factor),  $A$ , has units of [s<sup>-1</sup>], the temperature dependency exponent,  $B$ , is dimensionless, while the activation energy,  $E$ , is given here in [cal/mole].

## ILES framework

The computational study is based on the CFD code CNS3D (Compressible Navier-Stokes Solver in 3D)<sup>25–27</sup>. The code uses the finite volume (upwind) Godunov method in conjunction with several approximate Riemann solvers, written in Fortran 2008. It includes high-resolution methods of up to 11<sup>th</sup>-order of accuracy in space and 4<sup>th</sup>-order accuracy in time.

CNS3D can be used for implicit Large Eddy Simulations (iLES) and Direct Numerical Simulations (DNS)<sup>12,28–30</sup>. There is also a Reynolds-Averaged Navier-Stokes (RANS) version of the code. The focus, however, of the present and future developments is on iLES, which provide the best approach between accuracy and computational cost for any kind of engineering geometry. In classical Large Eddy Simulations (LES), the smallest length scales, which are the most computationally expensive to resolve, are removed via low-pass filtering of the Navier–Stokes equations. Then, the unresolved scales of turbulence are modeled by subgrid-scale models. In iLES, the computational grid removes small scales. The modelling of the unresolved scales is obtained through the non-linear dissipation embedded onto the high-resolution and high-order numerical schemes used to discretize the convective terms. There is a significant body of work in the literature, both theoretical and numerical, explaining iLES methods and demonstrating their accuracy in turbulent flows, e.g., see the books<sup>31,32</sup>.

In the present study, the HLLC solver is used in conjunction with a modified WENO 11<sup>th</sup>-order scheme<sup>12</sup>. High-order WENO schemes have proven resilient to the low-Mach number dissipation associated with compressible solvers<sup>33,34</sup> in contrast to Monotonic Upstream-centered Scheme for Conservation Laws (MUSCL) type schemes<sup>35</sup>, which generally require a low-Mach number treatment such as that proposed by Thornber, Mosedale, Drikakis, Youngs and Williams<sup>36</sup> (briefly described in the following section).

## Overview of numerical schemes

We employ the block-structured grid code CNS3D that solves the Navier–Stokes equations using the finite-volume method (FVM). The advective terms are solved using the Godunov-type (upwind) method, whose inter-cell numerical fluxes are calculated by solving the Riemann problem using the reconstructed values of the primitive variables at the cell interfaces. A one-dimensional swept unidirectional stencil is used for spatial reconstruction. The variables reconstruction is carried out accordingly<sup>37,38</sup>, to avoid spurious numerical oscillations from occurring at the interfaces between fluids of different heat capacity ratios ( $\gamma_i \neq \gamma_j$ ) due to the use of the four-equation model or otherwise the conservative mass-fraction transport equation

(Eq. (6), diffuse-interface method)<sup>39</sup>.

We have used a modified Weighted Essentially Non-Oscillatory (WENO) scheme, 11<sup>th</sup> order (W11), which we describe below. We also use a second-order central scheme for the viscous terms. The solution is advanced in time using a five-stage (fourth-order accurate) optimal strong-stability-preserving Runge–Kutta method<sup>40</sup>. Further details about the code can be found in Refs. <sup>12,33,34</sup> and references therein.

### Modified WENO Method

To address potential numerical instabilities due to the process of choosing an essentially non-oscillatory (ENO) stencil<sup>41</sup>, Weighted ENO (WENO) methods were introduced<sup>42,43</sup>. WENO schemes use a convex combination of all the ENO candidate stencils. Thus, the numerical flux is approximated by higher-order accuracy in smooth regions while still retaining the ENO property in the flow regions near discontinuities; see<sup>44,45</sup> for an overview and further references. For WENO implementations on structured grids, when the solution is locally smooth enough, the convex combination of the stencils of a  $r^{\text{th}}$ -order ENO scheme results in a  $(2r - 1)^{\text{th}}$ -order WENO scheme<sup>42</sup>.

Aiming to achieve a balance between accuracy and stability, we enhance the WENO schemes of 3<sup>rd</sup> and 5<sup>th</sup>-order of Jiang and Shu<sup>43</sup> ( $r = 2, 3$ ) and 7<sup>th</sup>, 9<sup>th</sup> and 11<sup>th</sup>-order of Balsara and Shu<sup>46</sup> ( $r = 4, 5, 6$ ) by combining the mapped WENO approach of Henrick, Aslam and Powers<sup>47</sup> (WENO-M) and the relative total variation limiter approach of Taylor, Wu and Martín<sup>48</sup> (WENO-RLTV). WENO-M recovers the loss of accuracy occurring near smooth critical points. WENO-RLTV reduces the numerical dissipation using the optimal linear weights in regions sufficiently smooth instead of the nonlinear smoothness-indicator-based weights. The numerical reconstruction can be performed at the level of conservative, characteristic, or primitive variables. The reconstruction of the conservative variables is more common in the literature. However, past research has shown that such practice can lead to inaccuracies in capturing shock waves; see Zanotti and Dumbser<sup>49</sup> and references therein. Like other authors<sup>50</sup>, we have opted to use the primitive variables in the high-order numerical reconstruction. The characteristics-based variables would be more expensive computationally.

We present below a step-by-step description of the WENO procedure implemented to obtain the left reconstruction,  $q_{i+1/2}^L$ , of the primitive variables,  $q = [\rho, \mathbf{u}, p]^T$ , at cell face  $i + 1/2$ :

1. The *full* (left and right reconstruction) stencil  $(S_{i+1/2}^G)$  is normalized, per variable, according to the transformation function:

$$S_{i+1/2}^{Gz} = \frac{S_{i+1/2}^G - g_{\min}}{g_{\max}} \quad (22)$$

where

$$S_{i+1/2}^G = (q_{i-r+1}, \dots, q_{i+r})$$

and

$$g_{\min} = \min(S_{i+1/2}^G) - 1, \quad g_{\max} = \max(S_{i+1/2}^G - q_{\min})$$

while the new  $k^{\text{th}}$  candidate stencil for the left reconstruction, containing  $r$  cell center values, is given by:

$$S_{i+1/2;k}^L = S_{i+1/2}^{Gz} [i - r + 1 + k, \dots, i + k],$$

where  $k = 0, \dots, r - 1$ . Eq. (22) simply normalizes the values of the candidate stencils prior to the estimation of the smoothness indicators ( $IS$ ) in such a way that (i) the maximum value of the full stencil becomes equal to one, i.e.,  $\max(S_{i+1/2}^{Gz}) = 1$ , (ii) the minimum value takes a positive and nonzero value, i.e.  $\min(S_{i+1/2}^{Gz}) > 0$ , and (iii) the value range scales as originally relative to the maximum. By definition  $g_{\max}$  is always positive and non-zero and hence Eq. (22) will never result in an undefined operation and cause an exception. Using the above *normalization* of the *full stencil values*, per variable, is found to (i) prevent negative WENO smoothness indicator values, (ii) reduce numerical dissipation, and (iii) simplify the application of the proceeding step. The stencil normalization was found to have no effect on the MUSCL-type slope limiters.

2. Next, a modified version of the relative total variation (TV) limiting procedure<sup>48</sup> is implemented. The TV of each  $k^{\text{th}}$  candidate stencil is calculated according to:

$$\text{TV}_k(S_{i;k}) = \sum_{l=1}^{r-1} |q_{i-r+k+l+1} - q_{i-r+k+l}| \quad (23)$$

Eq. (23) is then used to obtain the maximum TV ratio between the candidate stencils:

$$R(\text{TV}) = \frac{\max(\text{TV}_k)}{\min(\text{TV}_k) + \varepsilon} \quad (24)$$

If all of the stencils contain significant discontinuities, then the value of  $R(\text{TV})$  can be incorrectly small, i.e.  $R(\text{TV}) \approx 1$ . Thus, an additional criteria is introduced in order to avoid such a situation. The linear weights are used provided the following two conditions are satisfied:

$$\begin{aligned} &\text{if } \left[ R(\text{TV}) < A_{\text{RL}}^{\text{TV}} \ \& \right. \\ &\quad \left. \max(\text{TV}_k) < B_{\text{RL}}^{\text{TV}} \right] \text{ then} \\ &\quad \omega_k^r = C_k^r \end{aligned} \quad (25)$$

According to Ref.<sup>48</sup>,  $A_{\text{RL}}^{\text{TV}} = 5$ , while for the second condition,  $B_{\text{RL}}^{\text{TV}} = 0.2(r-1)$ , where  $r$  is the order of the polynomials used in the  $2(r-1)$ <sup>th</sup>-order WENO. Note that the equation for  $B_{\text{RL}}^{\text{TV}}$  is applicable only if the preceding pre-treatment/re-scaling of the candidate stencils is carried out; otherwise it must be multiplied by  $q_{\text{max}}$ . In essence, the second condition allows for an average TV of 20% between two neighbouring cells of the local stencils ( $S_i^r$ ) maximum variable value, but this value can be modified if necessary. Wu and Martín<sup>51</sup> used a value of  $B_{\text{RL}}^{\text{TV}} = 0.2$  for their 4<sup>th</sup>-order bandwidth-optimized WENO implementation in their DNS study.

Eq. (25) assumes that for the linear weights the condition  $\sum_{l=0}^{r-1} C_l^r = 1$  is always satisfied.

3. If condition Eq. (25) is not satisfied, then the nonlinear weights based on the smoothness indicators of each candidate stencil are computed according to the following two steps:

$$\Omega_k^r = \frac{C_k^r}{(\text{IS}_k^r)^p + \varepsilon}, \quad \omega_k^r = \frac{\Omega_k^r}{\sum_{l=0}^{r-1} \Omega_l^r}, \quad (26)$$

where  $p = r$  and  $\varepsilon = 10^{-41}$ .

The standard WENO weights obtained in Eq. (26) are modified according to the mapped WENO (WENO-M) approach<sup>47</sup> as:

$$\tilde{\omega}_k^r = \frac{\tilde{\Omega}_k^r}{\sum_{l=0}^{r-1} \tilde{\Omega}_l^r}, \quad (27)$$

where, using the alternate formulation of Feng, Huang and Wang<sup>52</sup>, the mapped weights are given by:

$$\tilde{\Omega}_k^r = C_k^r + \frac{(\Omega_k^r + C_k^r)^{K+1} A}{(\Omega_k^r - C_k^r)^K A + \Omega_k^r (1 - \Omega_k^r)} \quad (28)$$

and setting  $A = 1$  and  $K = 2$  results in the original mapping function<sup>47</sup>.

4. The reconstructed scaled variable value at the left-side of cell-face  $i + 1/2$  is given by:

$$q_{i+1/2}^L = \sum_{k=0}^{r-1} \left[ \tilde{\omega}_k^r f(q)_k^r \right], \quad (29)$$

where

$$f(q)_k^r = \sum_{l=0}^{r-1} \alpha_{k;l}^r q_{i-r+k+l+1} \quad (30)$$

5. Finally, due to the initial “normalizing” of the stencil in step 1, the reconstructed values obtained using Eq. (29) needs to be “re-scaled” according to:

$$q_{i+1/2}^L = q_{i+1/2}^L g_{\text{max}} + g_{\text{min}} \quad (31)$$

WENO reconstruction can lead to spurious oscillations, if two or more shocks are too close to each other and WENO cannot choose a single smooth stencil. To remedy this problem a procedure first introduced by Harten, Engquist, Osher and Chakravarthy<sup>53</sup> is adopted. If the reconstructed density and pressure values differ too drastically from their cell-center average values, the order of the WENO reconstruction is reduced. After completion of the left and right reconstruction procedures at cell-face  $i + 1/2$ , the left and right reconstructed density and pressure values are compared against their respective left and right cell-center values:

$$\begin{aligned} \left| \rho_{i+1/2}^L - \rho_i \right| &> C_{\theta}^- \quad \text{or} \\ \left| \rho_{i+1/2}^R - \rho_{i+1} \right| &> C_{\theta}^- \end{aligned} \quad (32)$$

, where the order reduction threshold constant is set equal to  $C_{\theta}^- = 0.7$ . If the condition in Eq. (32) is met, then the order of the WENO scheme is reduced according to  $(r - 1)$ . The reconstruction procedure is then repeated for all variables, and the condition is checked again. The process is repeated until Eq. (32) is not satisfied any longer. For example, assuming the condition is repeatably met, a 9<sup>th</sup>-order WENO would first reduce to 7<sup>th</sup>-order, then to 5<sup>th</sup>, 3<sup>rd</sup>, and finally to the 2<sup>nd</sup>-order MC MUSCL scheme. Titarev and Toro<sup>54</sup> showed that the use of the above procedure does not degrade the high order of accuracy for sufficiently smooth solutions.

As previously mentioned, for multi-component flows the following variables are reconstructed at the cell interfaces  $q = [\rho Y_j, \mathbf{u}, p]^T$ . However, WENO schemes do not adhere to the total variation diminishing (TVD) principle and are thus not monotonicity preserving. Consequently, conservation of the species mass-fractions is not guaranteed and nonphysical values can arise, i.e., negative or greater than one mass-fraction values. Therefore, following the WENO reconstruction of each  $j$ -th species mass,  $\rho Y_j$ , the obtained cell interface value is used to compute the *equivalent* MUSCL-scheme flux limiter,  $\psi'(r_i)$  according to:<sup>55</sup>:

$$\psi'(r_i) = 2 \left( q_{i+1/2}^L - q_i \right) / (\Delta_-)_i \quad (33)$$

where  $r_i = \Delta_+ / \Delta_-$ ,  $\Delta_- = q_i - q_{i-1}$  and  $\Delta_+ = q_{i+1} - q_i$ . The equivalent flux limiter value is then “limited” such to remain within the admissible limiter region for TVD schemes according to<sup>56</sup>:

$$\psi(r_i) = \max \left[ 0, \min \left( 2, 2r, \psi'(r_i) \right) \right] \quad (34)$$

The final reconstructed cell interface value of the species mass is then obtained by substituting in Eq. (33)  $\psi'$  with  $\psi$  and solving for  $q_{i+1/2}^L$ .

### Compressible filters

The accuracy of the present numerical schemes, and other methods, can be further enhanced in low-speed subsonic conditions by implementing a low-Mach correction<sup>36</sup> (henceforth labelled LMC). The low-Mach correction primarily involves an additional computational step that treats the velocity vector via a progressive central differencing of its components. The LMC ensures a balanced distribution of dissipation of kinetic energy in the limit of zero Mach number, thus extending the validity of compressible flow codes to Mach numbers as low as  $10^{-5}$ , and is mainly required for schemes providing accuracy less than 5<sup>th</sup>-order<sup>33,34</sup>.

After the reconstruction of the velocities has been carried out, the reconstructed left and right velocity components at cell-face  $(i + 1/2)$  are modified according to:

$$\mathbf{u}_{i+1/2}^{L,new} = (\mathbf{u}_s - \mathbf{u}_u) / 2, \quad \mathbf{u}_{i+1/2}^{R,new} = (\mathbf{u}_s + \mathbf{u}_u) / 2 \quad (35)$$

where

$$\mathbf{u}_s = \mathbf{u}_{i+1/2}^L + \mathbf{u}_{i+1/2}^R, \quad \mathbf{u}_u = \left( \mathbf{u}_{i+1/2}^L - \mathbf{u}_{i+1/2}^R \right) M_{\max} \quad (36)$$

and the maximum local Mach number is given by  $M_{\max} = \max \left( M_{i+1/2}^L, M_{i+1/2}^R \right)$ .

Note that the density and pressure are not altered in any way during this step, thus the internal energy component ( $\rho e = p / (\gamma - 1)$ ) remains unchanged. The reconstructed left and right total energies ( $e_t = e + e_k$ ) are calculated using the modified velocities in the kinetic energy component ( $e_k = \mathbf{u} \cdot \mathbf{u} / 2$ ).

### Details of the HLLC Riemann solver

The Riemann problem is solved here using the so-called ‘‘Harten, Lax, van Leer, and (the missing) Contact’’ (HLLC) approximate Riemann solver of Toro, Bruce and Spears<sup>57</sup>. More specifically, the adaptive non-iterative Riemann solver (ANRS) variant proposed by Toro<sup>58</sup> (see §9.5.2) is implemented. The following sequence details the approximate HLLC Riemann solver procedure implemented:

1. To ensure high-order near the boundaries for high-order FVM codes, typically, the ghost-cell method is used to apply the boundary conditions (BC). However, even after careful programming of the boundary conditions and reconstruction procedures, computer rounding errors can persist and give rise to differences between the left and right reconstructed states. Therefore, to ensure the appropriate flux, we modify the left and right reconstructed states for the following BCs: symmetry plane (inviscid wall), heated (constant temperature) wall, and adiabatic (zero heat-flux) viscous (no-slip) wall. For a symmetry plane, the no penetration condition is implemented for both advective and acoustic waves using the procedure described by Algorithm 1.

```

if Left BC Symmetry then
     $\rho_L = \rho_R;$ 
     $p_L = p_R;$ 
     $\mathbf{u}_R = \mathbf{u}_R - (\mathbf{u}_R \cdot \hat{\mathbf{n}})\mathbf{u}_R;$ 
     $\mathbf{u}_L = \mathbf{u}_R;$ 
else if Right BC Symmetry then
     $\rho_R = \rho_L;$ 
     $p_R = p_L;$ 
     $\mathbf{u}_L = \mathbf{u}_L - (\mathbf{u}_L \cdot \hat{\mathbf{n}})\mathbf{u}_L;$ 
     $\mathbf{u}_R = \mathbf{u}_L;$ 

```

**Algorithm 1:** Ensure symmetry BC flux in HLLC.

```

if Left BC Viscous Wall then
     $p_L = p_R;$ 
    if Wall Temperature then
         $\rho_R = p_R / (R_s T_W);$ 
         $\rho_L = \rho_R;$ 
         $\mathbf{u}_L = \mathbf{u}_R = 0;$ 
    else if Right BC Viscous Wall then
         $p_R = p_L;$ 
        if Wall Temperature then
             $\rho_L = p_L / (R_s T_W);$ 
             $\rho_R = \rho_L;$ 
             $\mathbf{u}_L = \mathbf{u}_R = 0;$ 

```

**Algorithm 2:** Ensure viscous wall BC flux in HLLC; if *Wall Temperature* true isothermal, else adiabatic.

In the case of a viscous wall, Algorithm 2 is used instead. For an isothermal wall, the temperature at the ghost cells is linearly interpolated from the interior domain and the wall. In this case, it is advisable to restrict the interpolated temperature range of values to be only positive ( $T \in \mathbb{R}_{>0}$ ), i.e.  $T_{\text{ghosts}} > 10^{-15}$ , which reduces the likelihood of a non-physical solution from manifesting.

2. An initial estimate of the pressure in the *Star Region*, that is the region defined in-between the two non-linear convective wave-speeds (or characteristics), can be obtained according to<sup>59</sup>:

$$p_* = \max(0, p_{\text{pvrs}}) \quad (37)$$

which for curvilinear coordinates  $p_{\text{pvrs}}$  is obtained according to:

$$p_{\text{pvrs}} = \frac{1}{2} \left[ p_L + p_R + \left( u_L^\perp - u_R^\perp \right) \bar{\rho} \bar{s} \right] \quad (38)$$

$$\bar{\rho} = (\rho_L + \rho_R) / 2, \quad \bar{s} = (s_L + s_R) / 2,$$

where the speed of sound is defined as  $s = \sqrt{\gamma p / \rho}$  and  $u^\perp = \mathbf{u} \cdot \hat{\mathbf{n}}$  is the magnitude of the velocity normal to the cell-face.

The ‘‘averaged’’ value of  $p_*$  given by Eq. (37), is enhanced by taking into account the local conditions. The ANRS approach<sup>58</sup> introduces two conditions as a means to avoid unnecessary computations, i.e. updating the value of  $p_*$  obtained by Eq. (37) with one that is more accurate. The first condition requires that the ratio between the maximum and minimum local reconstructed pressures is greater than a predetermined constant, i.e.

$$Q = p_{\text{max}} / p_{\text{min}} > Q_{\text{user}},$$

where  $p_{\text{min}} = \min(p_L, p_R)$ ,  $p_{\text{max}} = \max(p_L, p_R)$  and it is recommended that  $Q_{\text{user}} = 2$ . The other condition requires that  $p_*$  does not lie between  $p_{\text{min}}$  and  $p_{\text{max}}$ , i.e.  $p_* < p_{\text{min}}$  or  $p_* > p_{\text{max}}$ . However, akin to non-differentiable (reconstruction)

limiters, use of  $Q_{\text{user}}$  hinders the convergence in steady-state simulations. Instead, the following relation is used immediately after Eq. (37):

$$p_* = \begin{cases} \left[ \frac{s_L + s_R - \frac{\gamma-1}{2} (u_R^\perp - u_L^\perp)}{s_L/p_L^z + s_R/p_R^z} \right]^{\frac{1}{z}} & \text{if } p_* \leq p_{\min} \quad (\text{TRRS}) \\ \frac{g_L p_L + g_R p_R - (u_R^\perp - u_L^\perp)}{g_L + g_R} & \text{if } p_* > p_{\max}, \quad (\text{TSRS}) \end{cases}$$

where

$$z = \frac{\gamma-1}{2\gamma}, \quad A_K = \frac{2}{(\gamma-1)\rho_K}, \quad B = \left( \frac{\gamma-1}{\gamma+1} \right) p_K, \quad g_K = \left( \frac{A_K}{p + B_K} \right)^{1/2}, \quad K = L, R$$

The abbreviations TRRS<sup>58</sup> and TSRS<sup>58,60</sup> stand for the Two-Rarefaction Riemann Solver and Two-Shock Riemann Solver, respectively.

- Next, we compute the wave-speed estimates according to a modified formulation which combines the approaches of Davis<sup>61</sup> and Toro et al<sup>57</sup>:

$$S_L = \min \left( u_L^\perp - s_L q_L, u_R^\perp - s_R q_R \right), \quad S_R = \max \left( u_L^\perp + s_L q_L, u_R^\perp + s_R q_R \right), \quad (39)$$

where

$$q_K = \begin{cases} 1 & \text{if } p_* \leq p_K \\ \left[ 1 + \frac{\gamma+1}{2\gamma} \left( \frac{p_*}{p_K} - 1 \right) \right]^{1/2} & \text{if } p_* > p_K \end{cases} \quad (40)$$

Eq. (39) slightly increases the numerical diffusion as it permits a greater range, but has favourable stability in very high-speed flows and particularly near strong shock-waves.

The intermediate “missing” wave-speed ( $S_*$ ) can now be obtained by the following relation:

$$S_* = \frac{p_R - p_L + \rho_L u_L^\perp (S_L - u_L^\perp) - \rho_R u_R^\perp (S_R - u_R^\perp)}{\rho_L (S_L - u_L^\perp) - \rho_R (S_R - u_R^\perp)}$$

- Finally, the HLLC flux can be obtained by any of the variants given<sup>58</sup>. Here, the HLLC fluxes are estimated according to *Variant 1* (see § 10.6):

$$\mathbf{F}_{i+1/2}^{\text{hllc}} = \begin{cases} \mathbf{F}_L & \text{if } 0 \leq S_L \\ \mathbf{F}_{*L} & \text{if } S_L < 0 \leq S_* \\ \mathbf{F}_{*R} & \text{if } S_* \leq 0 < S_R \\ \mathbf{F}_R & \text{if } S_R \leq 0 \end{cases}, \quad (41)$$

where

$$\mathbf{F}_{*K} = \frac{S_* (S_K \mathbf{U}_K - \mathbf{F}_K) + S_K [p_K + \rho_K (S_K - u_K^\perp) (S_* - u_K^\perp)] \mathbf{D}_*}{S_K - S_*}$$

$$\mathbf{D}_* = [0, \hat{n}_x, \hat{n}_y, \hat{n}_z, S_*]^T$$

and

$$\mathbf{U} = \begin{bmatrix} \rho \\ \rho u \\ \rho v \\ \rho w \\ \rho e \end{bmatrix}, \quad \mathbf{F} = \begin{bmatrix} \rho u^\perp \\ \rho u u^\perp + p \hat{n}_x \\ \rho v u^\perp + p \hat{n}_y \\ \rho w u^\perp + p \hat{n}_z \\ (\rho e + p) u^\perp \end{bmatrix}$$

Using the above, the intermediate “missing” wave-speed,  $S_*$ , and associated HLLC fluxes are computed according to Toro<sup>58</sup>.

## References

1. Heiser, W., Pratt, D., Daley, D. & Mehta, U. *Hypersonic Airbreathing Propulsion* (American Institute of Aeronautics and Astronautics, 1994).
2. Xu, H. *et al.* Flight of an aeroplane with solid-state propulsion. *Nature* **563**, 532–535, DOI: [10.2514/2.5879](https://doi.org/10.2514/2.5879) (2018).
3. Toniato, P. *Free-jet testing of a Mach 12 scramjet in an expansion tube*. Ph.D. thesis, The University of Queensland (2019). DOI: [10.14264/uql.2019.342](https://doi.org/10.14264/uql.2019.342).
4. Nilsson, T., Zhong, S. & Fureby, C. LES of H<sub>2</sub>-air jet combustion in high enthalpy supersonic crossflow. *Phys. Fluids* **33**, 035133, DOI: [10.1063/5.0040398](https://doi.org/10.1063/5.0040398) (2021).
5. Zhao, X. *et al.* Research progress on solid-fueled scramjet. *Chin. J. Aeronaut.* DOI: [10.1016/j.cja.2021.06.002](https://doi.org/10.1016/j.cja.2021.06.002) (2021).
6. Chapuis, M. *et al.* A computational study of the HyShot II combustor performance. *Proc. Combust. Inst.* **34**, 2101–2109, DOI: <https://doi.org/10.1016/j.proci.2012.07.014> (2013).
7. Dai, J., Xu, F., Cai, X. & Mahmoudi, Y. Effects of velocity shear layer on detonation propagation in a supersonic expanding combustor. *Phys. Fluids* **33**, 105110, DOI: [10.1063/5.0065348](https://doi.org/10.1063/5.0065348) (2021).
8. Lee, W.-S. & Pan, K.-L. Computational investigation of an ethylene-fueled supersonic combustor assisted by a porous cylindrical burner. *Aerosp. Sci. Technol.* **107**, 106350, DOI: [10.1016/j.ast.2020.106350](https://doi.org/10.1016/j.ast.2020.106350) (2020).
9. Drummond, J. P. Methods for prediction of high-speed reacting flows in aerospace propulsion. *AIAA J.* **52**, 465–485, DOI: [10.2514/1.J052283](https://doi.org/10.2514/1.J052283) (2014).
10. Alff, F., Böhm, M., Clauß, W., Oschwald, M. & Waidmann, W. Supersonic combustion of hydrogen/air in a scramjet combustion chamber. In *45th International Astronautical Congress; 9th - 14th Oct., 1994; Jerusalem; Israel*, IAF 94-S.4.429 (1994).
11. Rana, Z. A., Thornber, B. & Drikakis, D. Transverse jet injection into a supersonic turbulent cross-flow. *Phys. Fluids* **23**, 046103, DOI: [10.1063/1.3570692](https://doi.org/10.1063/1.3570692) (2011).
12. Kokkinakis, I., Drikakis, D., Ritos, K. & Spottswood, S. M. Direct numerical simulation of supersonic flow and acoustics over a compression ramp. *Phys. Fluids* **32**, 066107, DOI: [10.1063/5.0010548](https://doi.org/10.1063/5.0010548) (2020).
13. Ritos, K., Drikakis, D. & Kokkinakis, I. W. Wall-pressure spectra models for supersonic and hypersonic turbulent boundary layers. *J. Sound Vib.* **443**, 90 – 108, DOI: [10.1016/j.jsv.2018.11.001](https://doi.org/10.1016/j.jsv.2018.11.001) (2019).
14. Ritos, K., Kokkinakis, I. W. & Drikakis, D. Physical insight into the accuracy of finely-resolved iLES in turbulent boundary layers. *Comput. & Fluids* **169**, 309 – 316, DOI: [10.1016/j.compfluid.2017.07.018](https://doi.org/10.1016/j.compfluid.2017.07.018) (2018).
15. Berglund, M. & Fureby, C. LES of supersonic combustion in a scramjet engine model. *Proc. Combust. Inst.* **31**, 2497–2504, DOI: [10.1016/j.proci.2006.07.074](https://doi.org/10.1016/j.proci.2006.07.074) (2007).
16. Potturi, A. & Edwards, J. LES/RANS simulation of a supersonic combustion experiment. In *50th AIAA Aerospace Sciences Meeting including the New Horizons Forum and Aerospace Exposition*, DOI: [10.2514/6.2012-611](https://doi.org/10.2514/6.2012-611) (2012).
17. Cao, C., Ye, T. & Zhao, M. Large eddy simulation of hydrogen/air scramjet combustion using tabulated thermo-chemistry approach. *Chin. J. Aeronaut.* **28**, 1316–1327, DOI: [10.1016/j.cja.2015.08.008](https://doi.org/10.1016/j.cja.2015.08.008) (2015).
18. Huang, Z., He, G., Qin, F. & Wei, X. Large eddy simulation of flame structure and combustion mode in a hydrogen fueled supersonic combustor. *Int. J. Hydrog. Energy* **40**, 9815–9824, DOI: [10.1016/j.ijhydene.2015.06.011](https://doi.org/10.1016/j.ijhydene.2015.06.011) (2015).
19. Wu, K., Zhang, P., Yao, W. & Fan, X. Numerical investigation on flame stabilization in DLR hydrogen supersonic combustor with strut injection. *Combust. Sci. Technol.* **189**, 2154–2179, DOI: [10.1080/00102202.2017.1365847](https://doi.org/10.1080/00102202.2017.1365847) (2017).
20. Banerjee, S., Krahl, R., Durst, F. & Zenger, C. Presentation of anisotropy properties of turbulence, invariants versus eigenvalue approaches. *J. Turbul.* **8**, N32, DOI: [10.1080/14685240701506896](https://doi.org/10.1080/14685240701506896) (2007).
21. Emory, M. & Iaccarino, G. Visualizing turbulence anisotropy in the spatial domain with componentality contours. In *Center for Turbulence Research, Stanford University, Annual Research Briefs*, 123–138 (Stanford University, 2014).
22. Karantonis, K., Kokkinakis, I. W., Thornber, B. & Drikakis, D. Compressibility in suddenly expanded subsonic flows. *Phys. Fluids* **33**, 105106, DOI: [10.1063/5.0065257](https://doi.org/10.1063/5.0065257) (2021).
23. Cook, A. W. Enthalpy diffusion in multicomponent flows. *Phys. Fluids* **21**, 055109, DOI: [10.1063/1.3139305](https://doi.org/10.1063/1.3139305) (2009).
24. Anderson, W. R., McQuaid, M. J., Nusca, M. J. & Kotlar, A. J. A detailed, finite-rate, chemical kinetics mechanism for monomethylhydrazine-red fuming nitric acid systems. Tech. Rep. ARL-TR-5088, Army Research Laboratory, Aberdeen Proving Ground, MD 21005-5066 (2010). Weapons and Materials Research Directorate, ARL.

25. Drikakis, D. & Tsangaris, S. On the solution of the compressible Navier–Stokes equations using improved flux vector splitting methods. *Appl. Math. Model.* **17**, 282–297, DOI: [10.1016/0307-904X\(93\)90054-K](https://doi.org/10.1016/0307-904X(93)90054-K) (1993).
26. Drikakis, D. Embedded turbulence model in numerical methods for hyperbolic conservation laws. *Int. J. for Numer. Methods Fluids* **39**, 763–781, DOI: [10.1002/flid.328](https://doi.org/10.1002/flid.328) (2002).
27. Drikakis, D. Advances in turbulent flow computations using high-resolution methods. *Prog. Aerosp. Sci.* **39**, 405–424, DOI: [10.1016/S0376-0421\(03\)00075-7](https://doi.org/10.1016/S0376-0421(03)00075-7) (2003).
28. Drikakis, D., Hahn, M., Mosedale, A. & Thornber, B. Large eddy simulation using high-resolution and high-order methods. *Proc. Royal Soc. A* **367**, 2985–2997, DOI: [10.1098/rsta.2008.0312](https://doi.org/10.1098/rsta.2008.0312) (2009).
29. Ritos, K., Kokkinakis, I. W., Drikakis, D. & Spottswood, S. M. Implicit large eddy simulation of acoustic loading in supersonic turbulent boundary layers. *Phys. Fluids* **29**, 046101, DOI: [10.1063/1.4979965](https://doi.org/10.1063/1.4979965) (2017).
30. Ritos, K., Kokkinakis, I. W. & Drikakis, D. Physical insight into a Mach 7.2 compression corner flow. In *2018 AIAA Aerospace Sciences Meeting*, DOI: [10.2514/6.2018-1810](https://doi.org/10.2514/6.2018-1810) (2018).
31. Grinstein, F. F., Margolin, L. G. & Rider, W. J. *Implicit large eddy simulation: computing turbulent fluid dynamics* (Cambridge University Press, 2007).
32. Drikakis, D. & Geurts, B. J. *Turbulent Flow Computation*, vol. 66 (Springer Netherlands, 2002).
33. Kokkinakis, I. & Drikakis, D. Implicit large eddy simulation of weakly-compressible turbulent channel flow. *Comput. Methods Appl. Mech. Eng.* **287**, 229 – 261, DOI: [10.1016/j.cma.2015.01.016](https://doi.org/10.1016/j.cma.2015.01.016) (2015).
34. Tsoutsanis, P. *et al.* Comparison of structured and unstructured-grid, compressible and incompressible methods using the vortex pairing problem. *Comput. Methods Appl. Mech. Eng.* **293**, 207–231 (2015).
35. van Leer, B. Towards the ultimate conservative difference scheme. V. A second-order sequel to Godunov’s method. *J. Comput. Phys.* **32**, 101–136, DOI: [10.1016/0021-9991\(79\)90145-1](https://doi.org/10.1016/0021-9991(79)90145-1) (1979).
36. Thornber, B., Mosedale, A., Drikakis, D., Youngs, D. & Williams, R. An improved reconstruction method for compressible flows with low Mach number features. *J. Comput. Phys.* **227**, 4873 – 4894, DOI: [10.1016/j.jcp.2008.01.036](https://doi.org/10.1016/j.jcp.2008.01.036) (2008).
37. Kokkinakis, I., Drikakis, D., Youngs, D. & Williams, R. Two-equation and multi-fluid turbulence models for Rayleigh–Taylor mixing. *Int. J. Heat Fluid Flow* **56**, 233–250, DOI: [10.1016/j.ijheatfluidflow.2015.07.017](https://doi.org/10.1016/j.ijheatfluidflow.2015.07.017) (2015).
38. Kokkinakis, I. W., Drikakis, D. & Youngs, D. L. Modeling of Rayleigh–Taylor mixing using single-fluid models. *Phys. Rev. E* **99**, 013104, DOI: [10.1103/PhysRevE.99.013104](https://doi.org/10.1103/PhysRevE.99.013104) (2019).
39. Allaire, G., Clerc, S. & Kokh, S. A five-equation model for the simulation of interfaces between compressible fluids. *J. Comput. Phys.* **181**, 577–616, DOI: [10.1006/jcph.2002.7143](https://doi.org/10.1006/jcph.2002.7143) (2002).
40. Spiteri, R. & Ruuth, S. A new class of optimal high-order strong-stability-preserving time discretization methods. *SIAM J. on Numer. Analysis* **40**, 469–491, DOI: [10.1137/S0036142901389025](https://doi.org/10.1137/S0036142901389025) (2002).
41. Shu, C. W. Numerical experiments on the accuracy of ENO and modified ENO schemes. *J. Sci. Comput.* **5**, 127–149, DOI: [10.1007/BF01065581](https://doi.org/10.1007/BF01065581) (1990).
42. Liu, X.-D., Osher, S. & Chan, T. Weighted essentially non-oscillatory schemes. *J. Comput. Phys.* **115**, 200 – 212, DOI: [10.1006/jcph.1994.1187](https://doi.org/10.1006/jcph.1994.1187) (1994).
43. Jiang, G.-S. & Shu, C.-W. Efficient implementation of weighted ENO schemes. *J. Comput. Phys.* **126**, 202 – 228, DOI: [10.1006/jcph.1996.0130](https://doi.org/10.1006/jcph.1996.0130) (1996).
44. Shu, C.-W. Essentially non-oscillatory and weighted essentially non-oscillatory schemes for hyperbolic conservation laws. In Quarteroni, A. (ed.) *Advanced Numerical Approximation of Nonlinear Hyperbolic Equations: Lectures given at the 2nd Session of the Centro Internazionale Matematico Estivo (C.I.M.E.) held in Cetraro, Italy, June 23–28, 1997*, 325–432, DOI: [10.1007/BFb0096355](https://doi.org/10.1007/BFb0096355) (Springer Berlin Heidelberg, Berlin, Heidelberg, 1998).
45. Shu, C. High order weighted essentially nonoscillatory schemes for convection dominated problems. *SIAM Rev.* **51**, 82–126, DOI: [10.1137/070679065](https://doi.org/10.1137/070679065) (2009).
46. Balsara, D. S. & Shu, C.-W. Monotonicity preserving weighted essentially non-oscillatory schemes with increasingly high order of accuracy. *J. Comput. Phys.* **160**, 405 – 452, DOI: [10.1006/jcph.2000.6443](https://doi.org/10.1006/jcph.2000.6443) (2000).
47. Henrick, A. K., Aslam, T. D. & Powers, J. M. Mapped weighted essentially non-oscillatory schemes: Achieving optimal order near critical points. *J. Comput. Phys.* **207**, 542 – 567, DOI: [10.1016/j.jcp.2005.01.023](https://doi.org/10.1016/j.jcp.2005.01.023) (2005).

48. Taylor, E. M., Wu, M. & Martín, M. P. Optimization of nonlinear error for weighted essentially non-oscillatory methods in direct numerical simulations of compressible turbulence. *J. Comput. Phys.* **223**, 384 – 397, DOI: [10.1016/j.jcp.2006.09.010](https://doi.org/10.1016/j.jcp.2006.09.010) (2007).
49. Zanotti, O. & Dumbser, M. Efficient conservative ADER schemes based on WENO reconstruction and space-time predictor in primitive variables. *Comput. Astrophys. Cosmol.* **3**, 1–32, DOI: [10.1186/s40668-015-0014-x](https://doi.org/10.1186/s40668-015-0014-x) (2016).
50. Nichols, R. H., Tramel, R. W. & Buning, P. G. Evaluation of two high-order weighted essentially nonoscillatory schemes. *AIAA J.* **46**, 3090–3102, DOI: [10.2514/1.36849](https://doi.org/10.2514/1.36849) (2008).
51. Wu, M. & Martín, M. P. Direct numerical simulation of supersonic turbulent boundary layer over a compression ramp. *AIAA J.* **45**, 879 – 889, DOI: [10.2514/1.27021](https://doi.org/10.2514/1.27021) (2007).
52. Feng, H., Huang, C. & Wang, R. An improved mapped weighted essentially non-oscillatory scheme. *Appl. Math. Comput.* **232**, 453 – 468, DOI: [10.1016/j.amc.2014.01.061](https://doi.org/10.1016/j.amc.2014.01.061) (2014).
53. Harten, A., Engquist, B., Osher, S. & Chakravarthy, S. R. Uniformly high order accurate essentially non-oscillatory schemes, III. *J. Comput. Phys.* **131**, 3 – 47, DOI: [10.1006/jcph.1996.5632](https://doi.org/10.1006/jcph.1996.5632) (1997).
54. Titarev, V. & Toro, E. Finite-volume WENO schemes for three-dimensional conservation laws. *J. Comput. Phys.* **201**, 238 – 260, DOI: [10.1016/j.jcp.2004.05.015](https://doi.org/10.1016/j.jcp.2004.05.015) (2004).
55. Spekreijse, S. Multigrid solution of monotone second-order discretizations of hyperbolic conservation laws. *Math. Comput.* **49**, 135–155, DOI: [10.1090/S0025-5718-1987-0890258-9](https://doi.org/10.1090/S0025-5718-1987-0890258-9) (1987).
56. Sweby, P. K. High resolution schemes using flux limiters for hyperbolic conservation laws. *SIAM J. on Numer. Analysis* **21**, 995–1011, DOI: [10.1137/0721062](https://doi.org/10.1137/0721062) (1984).
57. Toro, E. F., Spruce, M. & Speares, W. Restoration of the contact surface in the HLL-Riemann solver. *Shock. Waves* **4**, 25 – 34, DOI: [10.1007/BF01414629](https://doi.org/10.1007/BF01414629) (1994).
58. Toro, E. F. *Riemann Solvers and Numerical Methods for Fluid Dynamics, A Practical Introduction* (Springer-Verlag Berlin Heidelberg, 2009), 3 edn.
59. Toro, E. F. A linearized Riemann solver for the time-dependent Euler equations of gas dynamics. *Proc. Royal Soc. London. Ser. A: Math. Phys. Sci.* **434**, 683–693, DOI: [10.1098/rspa.1991.0121](https://doi.org/10.1098/rspa.1991.0121) (1991).
60. Toro, E. F. Direct Riemann solvers for the time-dependent Euler equations. *Shock. Waves* **5**, 75, DOI: [10.1007/BF02425037](https://doi.org/10.1007/BF02425037) (1995).
61. Davis, S. Simplified second-order Godunov-type methods. *SIAM J. on Sci. Stat. Comput.* **9**, 445–473, DOI: [10.1137/0909030](https://doi.org/10.1137/0909030) (1988).

## Author contributions statement

I.W.K. and D.D. developed the computational methods used in the simulations over several years, I.W.K. performed the computations, post-processed the results and contributed to the writing of the paper, D.D. (jointly with I.W.K.) conceived the problem description, and furthermore contributed to the analysis of the results and writing of the paper; Y.Q.H. contributed to the implementation of the chemical reactions and the discussion of the results; G.Z.L. offered ideas about the scramjet technologies. All authors reviewed the manuscript.